https://doi.org/10.1016/j.engstruct.2019.01.029

A multi-stage-based nonlinear static procedure for estimating seismic demands of steel MRFs equipped with steel slit walls

Ke Ke[a,b,*], Fuming Wang[a], Michael CH Yam[b,c], Lu Deng[a], Yongjun He[a]

[a] *Hunan Provincial Key Laboratory for Damage Diagnosis of Engineering Structures, Hunan University, Changsha, China*

[b] *Department of Building and Real Estate, The Hong Kong Polytechnic University, Hong Kong, China*

[c] *Chinese National Engineering Research Centre for Steel Construction (Hong Kong Branch), The Hong Kong Polytechnic University, Hong Kong, China*

Abstract:

This paper aims to develop a nonlinear static procedure for estimating seismic demands of steel moment resisting frames (MRFs) equipped with steel slit walls (SSWs) exhibiting multi-yielding stages under seismic actions. The hysteretic behaviour of a steel MRF equipped with SSWs was examined. Numerical models were also developed and verified by revisiting a previous full-scale test programme. The applicability of a classical trilinear kinematic model for idealising the hysteretic response of the systems was examined. Then, a multi-stage-based nonlinear static procedure (MNSP) governed by the energy-balance concept was proposed, which enables practitioners to quantify the seismic demands of a steel MRFs equipped with SSWs showing multi-yielding stages. The MNSP was subsequently applied to two prototype steel MRFs equipped with SSWs under design basis earthquakes and maximum considered earthquakes. The predictions by the MNSP were compared with nonlinear response history analysis (NL-RHA) to examine the effectiveness of the method. The lateral load distributions documented in FEMA-356 were also included in the work for comparison. The observations from this study suggests that the proposed MNSP offers a promising tool for estimating the peak seismic response of steel MRFs equipped with SSWs showing multi-yielding stages.

Keywords: steel slit wall, multi-yielding stages, pushover analysis, energy-based procedure, trilinear hysteretic model

* Corresponding author.
Email address: keke@hnu.edu.cn

1. Introduction

Recent post-earthquake structural damage evaluations have highlighted the limitations of the conventional seismic design methodology pursuing the ductility as the sole objective. For a steel moment resisting frame (MRF) designed following current seismic provisions, yielding of members and connections in rapid succession triggered by earthquake loading generally results in significant post-disaster structural damages and residual deformations [1-3], and hence long-time occupancy suspension is expected due to the repairing works. In cases where severe damages are sustained by a system, complete demolition-and-reconstruction is needed. Recognising that continuous operation and fast functional recovery of the system after a seismic event are critical for maintaining both economic prosperity and social stability, the research community engaged in seismic hazard mitigation has shifted the pursuit from 'life-safety' to 'performance-based design' [4, 5] and 'seismic resilience' [6, 7]. In this context, passive energy dissipation device (EDD) [8] is an attractive solution for enhancing the seismic behaviour of conventional ductile steel MRFs. With a wise design, EDDs can dissipate plastic energy at smaller deformation levels, and members of a MRF are able to respond elastically to produce the 'damage-control' behaviour [9-11].

Among newly emerged plate-type EDDs [12-14], the steel slit wall (SSW) [15-20] is a promising candidate and has drawn much attention from the research community. With slits distributed in a steel panel, a SSW resists lateral loading by bending behaviour of a series of flexural links, and a steel MRF with SSW is schematically shown in Fig. 1. The hysteretic performance of the SSWs and the steel MRFs equipped with SSWs as EDDs

have been examined by a number of researchers in recent decades. For instance, Hitaka and Matsui [15] examined the seismic performance of SSWs with various geometries and slit configurations based on an experimental and numerical study. The authors proposed design methods for calculating the lateral stiffness and ultimate strength of a SSW. Later, SSWs were applied in steel MRFs, and the ductile manner of the system in the extreme state was verified [16]. Gortes and Liu [21] developed a similar system combining the steel frames with steel slit panels, and the feasibility of the novel system was strengthened by a large experimental programme. He et al. [18] recently investigated the seismic performance of SSWs with low-yield-steel plate and proposed a design procedure for the SSWs. To examine the potential of using SSWs as sacrificial members under seismic attacks, Ke and Chen [22] conducted a feasibility-of-concept study on steel MRFs equipped with SSWs using full-scale quasi-static tests. The earlier yielding of the SSW in the 'damage-control stage' and the synergetic energy dissipation behaviour of the SSW and the MRF in the 'ultimate stage' were observed. The multi-yielding stages of a steel MRF equipped with SSWs were in line with the fundamental requirements of the performance-based seismic engineering. More recently, Wang et al. [23] developed an innovative self-centring modular panel using the SSW as the energy dissipation member.

From the practical application point of view, quantification of seismic demands of steel MRFs equipped with SSWs subjected to expected earthquake events is an essential task for extending the system in seismic regions. In this respect, nonlinear static analysis procedures [24-26] are promising tools as they could shed insightful lights on the seismic demands of structures and can be used in the preliminary design or evaluations before

eventually transitioning to the most rigorous approach, i.e. the nonlinear history response analysis (NL-RHA). This study aims to develop a multi-stage-based nonlinear static analysis procedure for estimating the seismic demands of steel MRFs equipped with SSWs. The seismic demand quantification of the structure in both the damage-control stage where only SSWs yield and the ultimate stage with significant yielding of the steel MRF is employed in the procedure. First, the cyclic behaviour of steel MRFs equipped with SSWs was revisited, and numerical models were developed and verified by a recent full-scale test programme. The applicability of a multi-linear kinematic model for describing the nonlinear force-displacement response of steel MRFs equipped with SSWs was examined in detail. Then, the seismic energy balance of steel MRFs equipped with SSWs in multi-yielding stages was developed using the concept of the modal equivalent oscillator assigned with the verified hysteretic model. A stepwise multi-stage-based nonlinear static procedure (MNSP) was subsequently proposed, and it was applied to seismic demand evaluation of prototype steel MRFs equipped with SSWs. The rationality of the invariant lateral load distributions in the MNSP for quantifying the seismic demands of steel MRFs equipped with SSWs was strengthened by conducting a comparative study employing lateral load distributions documented in FEMA-356 [27]. The adequacy of the proposed procedure was justified using NL-RHAs of the prototype structures under two ensembles of earthquake ground motions representing design basis earthquakes and maximum considered earthquakes, respectively.

2. **Hysteretic characteristics of steel MRFs equipped with SSWs**

2.1. Test programme

Two full-scale tests on the seismic behaviour of steel MRFs equipped with SSWs have been conducted by Ke and Chen [22]. For both specimens, a SSW with the panel dimension of 2258 mm × 1970 mm (panel height × panel width) and the thickness of 12 mm was installed in a steel MRF with the dimension of 4750 mm × 3348 mm (bay length × storey height). An I-section beam of 400 × 200 × 8 × 13 (beam depth × beam width × web thickness × flange thickness, unit: mm) along with the cold formed-square tubular column of 350 × 350 × 12 (column depth × column width × thickness, unit: mm) was used in the MRF. The frame members (i.e. I-section beam and cold-formed square column) were made of grade Q345 steel with the nominal yield strength of 345 MPa, and the SSWs were fabricated from grade Q235 steel plates with the nominal yield strength of 235 MPa. The detailed information about the measured material properties from coupon tests can be found in [22]. The slits in the SSWs were cut by a 'SlabCO2' laser machine, and a slit width of 12 mm was used with the error ranging from 0.1 to 0.4 mm. The surface roughness was limited to a reasonable range (i.e. 12.5 μm to 25 μm). The end of the slits was rounded with the radius of 6 mm to avoid stress concentration. Two rows of flexural links with the designed aspect ratio (i.e. link length to link width ratio) ranging from 5.03 to 5.14 along with the width to thickness ratio (i.e. link width to panel thickness) ranging from 11.67 to 11.92 were produced in the SSW panels. Note that the configuration of the slits and the flexural links was in line with the design recommendations in previous works [15, 21]. The first specimen coded as 'FSSW1' was designed to simulate the subassembly of a MRF with a SSW in the ground floor, and hence the bottom beam was fixed on the ground. The other specimens 'FSSW2' corresponded to the scenario in which SSWs were

not consecutively arranged in all floors, and thus the effect of the flexibility of the girder in the lower floor was employed. An overview of the test programme is reproduced in Fig. 2.

2.2. Numerical modelling strategy and hysteretic behaviour of steel MRF equipped with SSWs

The finite element (FE) programme ABAQUS [28] was used to develop numerical models of the two specimens in the previous test programme [22]. Specifically, a SSW was discretised by linear quadrilateral four-node doubly curved thin shell elements with reduced integration (i.e. S4R elements). The two-node linear beam elements with first order interpolation (i.e. B31 elements) were utilised to model the frame members. Intersecting elastic B31 elements were used to simulate the connection between the SSW with the adjacent girders. Note that the adequacy of this modelling strategy for simulating the connections between the SSWs and the frame beams was verified in a previous work [29]. The mesh size for the SSWs and the MRF was approximately 20 mm, which was finalised using a trial-and-error procedure. An overview of the assembly of the FE models of the specimens is shown in Fig. 3. Different boundary conditions were included in the models for representation of the two specimens. In particular, the 'encastre' boundary condition was used for the lower beam in the model of specimen 'FSSW1' to produce a fixed end, i.e. U1=U2=U3=UR1=UR2=UR3=0, where U1, U2 and U3 represent the translational movement as shown in Fig. 3, while UR1, UR2 and UR3 are the corresponding rotational movement. Comparatively, only the bases of the stub column of the model for FSSW2 was fixed, and the rotational movement of the lower beam was

allowed. To replicate the support by the lateral bracing system in the test, lateral movements of the girder (U1=0) at the bracing points were restrained. The material nonlinearity for the SSWs and the frame components was included in the model based on elastic-plastic multi-linear simplification, i.e. kinematic model, governed by the von Mises yield criterion. The coupon test results were used to produce the input material properties. The geometric nonlinearities were also included in the FE models.

A three-step analysis procedure was adopted to reproduce the loading protocols in the quasi-static tests. Specifically, a buckling analysis was performed first to obtain the fundamental buckling mode of the SSW, and it was subsequently scaled and utilised as the initial geometric imperfection for the FE models. To investigate the effect of the magnitude of the initial imperfection on the cyclic response of the steel MRFs equipped with SSWs, a sensitivity analysis was conducted with two analysis cases in the second step. In 'case A', the amplitude of the initial imperfection of SSWs was specified according to Eurocode 3 [30]. In particular, the fundamental buckling mode was scaled, and the magnitude was set as $B_s/200$ = 9.9 mm, where B_s is the short span of the panel (i.e. the width of the SSW). In 'case B', the buckling restrained configuration was simulated by restraining the lateral movement of flexural links (U1). In each case, the constant vertical load applying on the upper girder of the specimens was included for simulating the gravity load applied on the specimen. In the third step, static analysis was performed and cyclic loads in accordance with the loading protocol of the quasi-static tests were applied on the FE models.

The FE simulation was compared with the test results till the load cycle where evident

134 cracking was initiated in SSWs (i.e. loading amplitude of 50 mm), as shown in Fig. 4. It is
135 seen that reasonable correlation between the FE predictions and the test results was
136 obtained, and the predicted curves by 'case A' were in better agreement with the test
137 results because the behaviour deterioration of the SSWs induced by distortional buckling
138 of the flexural links was simulated reasonably. In contrast, fuller hysteretic curves were
139 achieved in 'case B', in which the lateral distortional buckling of the flexural links was
140 avoided. In addition, the initial stiffness and the peak base shear (at the load cycle of 50
141 mm) by FE predictions are also compared with the test results, as indicated in Fig. 4. It can
142 be observed that FE predictions may slightly overestimate the initial stiffness and the
143 strength of the test specimens, and the response curves predicted by 'case B' have
144 relatively higher stiffness and ultimate base shear. These observations are also in line with
145 the research findings from recent experimental investigations. In particular, inception of
146 distortional buckling of flexural links in the SSWs is a major cause of cyclic deterioration
147 and an inducement to trigger early cracking of the panels. Therefore, the discussion of
148 steel MRFs equipped with SSWs in the following sections is based on the presumption that
149 a structure is well designed without inception of performance deterioration for a wide
150 deformation range. Cyclic degradation induced by distortional buckling of flexural links,
151 fracture of SSWs and local buckling of frame members were not included in the model. In
152 practical cases, available buckling restrained devices [21, 29] can ensure the stable
153 hysteretic performance of SSWs.
154
155 *2.3. Feasibility of a trilinear hysteretic model*

156 The pushover force-displacement response of a steel MRF with SSWs showing multi-
157 yielding stages can be characterised by typical trilinear behaviour, as schematically shown
158 in Fig. 1b. Note that The multi-yielding stages are formed owing to the yield deformation
159 gap between the SSWs and the MRF (i.e. $\delta_2 > \delta_1$, where δ_2 = yield deformation of the steel
160 MRF and δ_1 = yield deformation of the SSWs, respectively). In particular, a 'damage-
161 control core' (Fig. 5) governed by the bilinear kinematic hysteretic rule [22] can quantify
162 the force-displacement hysteretic response if the maximum deformation does not exceed
163 the equivalent yield deformation of the MRF, and the shape of the damage-control core is
164 quantified by two non-dimensional hysteretic quantities, i.e. the yield displacement ratio
165 ($\zeta_1=\delta_2/\delta_1$) and the post-yielding ratio in the damage-control stage (α_1). For a steel MRF
166 with SSWs progressing to the ultimate stage with evident inelastic actions triggered in
167 frame members, the hysteretic response can be idealised by a trilinear simplification. The
168 hysteretic model of the system is given in Fig. 5, and the loading-unloading-reloading path
169 is governed by reference lines (i.e. L_0~L_7 in Fig. 5 and Fig. 6). It is worth noting that the
170 loading-unloading-reloading path of a steel MRF equipped with SSWs depends on the
171 hysteretic characteristics of the damage-control core. Specifically, when the hysteretic
172 parameters of the damage-control core satisfy $\alpha_1(\zeta_1-1) >1$, yielding of SSWs is activated
173 during unloading, and the loading-unloading-reloading path is schematically shown in Fig.
174 6a. Otherwise, a fuller damage-control core is formed, and the loading-unloading-
175 reloading rule is illustrated in Fig. 6b. According to the hysteretic law, a steel MRF with
176 SSWs progressing to the ultimate stage is quantified by shifting of the damage-control
177 core, and the post-yielding stiffness ratio in the ultimate stage, i.e. α_2, governs the shifting

178 path of the damage-control core. To demonstrate this mechanism, the FE models for the
179 specimen 'FSSW1' and 'FSSW2' in case B (i.e. buckling restrained) was loaded under a
180 loading protocol with 'shifting action'. The analysis results were compared with the
181 trilinear idealisation, as given in Fig. 7, and reasonable agreement between the FE results
182 and the trilinear idealisation can be observed. Thus, the effectiveness of the trilinear
183 kinematic hysteretic model for describing the hysteretic behaviour of steel MRFs with
184 SSWs was demonstrated, and the model was used as the basis to explore the nonlinear
185 static procedure for prescribing seismic demands of the system subjected to expected
186 earthquake excitations.

187

188 **3. A stepwise multi-stage-based nonlinear static procedure**

189 *3.1. Seismic energy balance of steel MRFs equipped with SSWs in multi-yielding stages*

190 The energy-balance-concept-based seismic design was initiated by Housner [31] in the
191 last century, and the peak seismic response demand of a structure was directly related to
192 the elastic spectral pseudo-velocity or pseudo-acceleration of the equivalent oscillator.
193 Recently, it was observed that the inelastic action of a system interacts with earthquake
194 ground motion properties, and hence Lee et al. [32, 33] developed a modified energy-
195 based equation using the classical elasto-perfectly-plastic (EPP) model. An energy factor
196 was introduced into the classical Housner equation, reproduced as follows:

197 $$\gamma(\frac{1}{2}MS_v^2) = E_e + E_p \quad (1)$$

198 where γ = energy factor for modifying the Housner principle; M = mass of the oscillator; S_v
199 = pseudo-velocity; E_e = elastic energy defined by the elastic part covered by the area of the

skeleton pushover curve of an EPP system and E_p = plastic energy defined by the inelastic part covered by the pushover curve of an EPP system. The energy factor defined by the ratio of the covered area by the skeleton pushover response of the inelastic system and the horizontal coordinate axis to that of the correlated elastic oscillator was utilised to quantify the interactive effects between the nonlinear dynamic behaviour of the system and earthquake ground motion characteristics [32, 33].

The logic of the present study is in line with the modified Housner equation, i.e. Eq. (1), and the influence of the multi-yielding stages of the force-displacement responses on the seismic demand of a steel MRF with SSWs can be quantified by the energy factor. Note that a multi-storey steel MRF equipped with SSWs acts as a typical multi-degree-of-freedom (MDOF) system influenced by multi-modes, and modal combinations can be used to quantify the energy balance of the structure. The energy factor of modal oscillators representing a steel MRF equipped with SSWs is demonstrated in Fig. 8. Specifically, utilising the hysteretic force-displacement characteristics of the system in the damage-control stage (Fig. 8a), the energy factor of a modal oscillator (i.e. the n^{th} mode) [34] is given by

$$\gamma_n = \chi[2\mu_n - 1 + \alpha_{1,n}(\mu_n - 1)^2] \tag{2}$$

$$\chi(T_n; \mu_n; \alpha_{1,n}; \xi_n) = (\frac{V_{1,n}}{V_{e,n}})^2 \tag{3}$$

where T_n = period; $\mu_n = \delta_n/\delta_{1,n}$ (where δ_n and $\delta_{1,n}$ are the maximum displacement under an earthquake motion and the displacement quantifying yielding of the SSWs, respectively.); $\alpha_{1,n}$ = post-yielding stiffness ratio of the damage-control core; $V_{1,n}$ = first yield force of the oscillator corresponding to yielding of the SSWs; $V_{e,n}$ = maximum force of the

corresponding elastic oscillator; ξ_n = damping ratio; χ = damage-control factor depending on the hysteretic parameters and nonlinear dynamic characteristics of the oscillator. Eqs (2)-(3) quantify the energy factor of the bilinear oscillator, and they are valid for cases $\delta_n < \delta_{2,n}$, where the modal oscillators are deforming in the damage-control stage.

Once yielding of the steel MRF is triggered and the system progresses to the ultimate stage (Fig. 8b), the trilinear hysteretic characteristics should be considered, and the energy factor can be quantified based on a trilinear idealisation [34], expressed as

$$\gamma_n^{'} = \chi[2\zeta_{1,n} - 1 + \alpha_{1,n}(\zeta_{1,n} - 1)(2\mu_n - \zeta_{1,n} - 1) + \alpha_{2,n}(\mu_n - \zeta_{1,n})^2] \quad (4)$$

$$\chi(T_n; \zeta_{1,n}; \mu_n; \alpha_{1,n}; \alpha_{2,n}; \xi_n) = (\frac{V_{1,n}}{V_{e,n}})^2 \quad (5)$$

where $\zeta_{1,n}$ = yield displacement ratio (i.e. $\zeta_{1,n} = \delta_{2,n}/\delta_{1,n}$, where $\delta_{2,n}$ is the yield displacement of a trilinear oscillator quantifying yielding of the steel MRF of the n^{th} mode.); As can be seen, the damage-control factor of the oscillator in the ultimate stage is influenced by additional parameters, i.e. $\alpha_{2,n}$ and $\zeta_{1,n}$. Note that the energy factor can be computed through a constant-ductility-based procedure with iterations, and more detailed information about the development of energy factor spectra of oscillators showing multi-yielding stages is documented in [34–36]. In summary, compared with the previous works established on the energy balance of the EPP model [32, 33], the energy factor accounting for the progressively yielding behaviour of steel MRFs equipped with SSWs can be utilised to quantify the influence of the hysteretic parameters on the energy balance of the system in various yielding stages. The MNSP was established using the energy factor as an essential index, and the detail will be discussed in later sections.

3.2. Underlying assumptions

In the MNSP, the modal oscillator analogy was used to estimate the peak seismic response demands of a steel MRF equipped with SSWs, and a step-by-step framework was developed. The assumptions of the procedure are clarified as follows: (1) The seismic action can be simplified with invariant lateral load distributions applied on the structure; (2) The coupling effect among the modal coordinates in terms of energy induced by yielding of the system is ignored when quantifying seismic demands of a multi-mode-sensitive steel MRF equipped with SSWs; (3) The SRSS superposition method [25, 37] of modal responses can be applied to the structure in the inelastic range. It is worth noting that the assumptions were adopted in recent works on nonlinear static pushover procedures, e.g. the widely used modal pushover analysis (MPA) method [25], and the feasibility will be further validated by demonstration of the MNSP in next sections.

3.3. Detail of the MNSP

Using the energy factor in the multi-yielding stages as the core demand index, the stepwise MNSP was developed and is presented as follows:

(1) Perform frequency analyses for essential vibration modes and extract the elastic vibration quantities of a steel MRF equipped with SSWs, i.e. the period T_n, the effective mass M_n^*, the modal vector $\boldsymbol{\varphi}_n$, and the participation factor Γ_n. Generally, the first two or three modes will be sufficient, and the modelling techniques discussed in Section 2 can be used for developing the structural model in case where effective buckling restraint SSWs are installed in a system.

(2) Conduct pushover analyses for the critical vibration modes using the lateral load distributions proposed by Chopra and Goel [25]:

$$\mathbf{L}_n = \mathbf{m}\boldsymbol{\varphi}_n \tag{6}$$

where $\mathbf{L}_n$ = lateral load distribution vector of the n^{th} mode; $\mathbf{m}$ = mass matrix; and $\boldsymbol{\varphi}_n$ = modal vector of the n^{th} mode.

(3) Develop the base shear versus the energy-based displacement responses and the energy capacity curves using the pushover database obtained in the previous step. Specifically, these response curves can be obtained by converting the force-displacement-based pushover responses, i.e. base shear versus roof displacement responses, into energy-based curves based on the approach proposed by Hernandez-Montes et al. [38-40]. The detailed formulas for producing the 'energy-based' responses are reproduced in **Appendix A**.

(4) Idealise the base shear versus energy-based displacement responses with a multi-linear idealisation, and the algorithm [3] is also reproduced in **Appendix A**. Hence, the hysteretic parameters of an energy-based modal oscillator (i.e. $\alpha_{1,n}$, $\alpha_{2,n}$, $\zeta_{1,n}$, and μ_n) can be computed. It is worth pointing out that a target displacement should be selected first during the curve idealisation, and a relatively large value can be used as a start point to launch an iterative process.

(5) Determine the energy factor of modal oscillators in multi-yielding stages based on Eqs. (2)-(5), and compute the energy demand curve based on the nonlinear hysteretic parameters of the base shear versus energy-based displacement responses, dynamic properties of the modal oscillators (T_n, ξ_n) and pseudo-velocity of the n^{th} mode ($S_{\text{v},n}$),

given by

$$E_{a,n} = \begin{cases} 1 & (\mu_n \le 1) \\ \gamma_n \left(\frac{1}{2} M_n^* S_{v,n}^2\right) & (1 < \mu_n \le \zeta_{1,n}) \\ \gamma_n' \left(\frac{1}{2} M_n^* S_{v,n}^2\right) & (\mu_n > \zeta_{1,n}) \end{cases} \quad (7)$$

(6) For the n^{th} mode, plot the energy demand curve and the corresponding capacity curve (step 3) in one diagram, and the peak response demand of the n^{th} mode is estimated by the intersecting point of the energy demand response curve and the corresponding capacity response curve acting as the 'performance point'. Therefore, the peak response demand quantities of the n^{th} mode (e.g. peak floor displacement, interstorey drift and roof drift) can be extracted from the analysis results when the modal oscillator reaches the performance point. Iterations may be needed to finalise the performance point (i.e. go back to step 4).

(7) Compute the seismic demand quantities of the entire structure using the SRSS superposition method using the demand quantities in the influential modes.

$$D = \sqrt{\sum_{n=1}^{N} \left(D_n^2\right)} \quad (8)$$

where D_n = demand quantities of the n^{th} mode, D = demand quantities of the entire system and N = the number of considered modes. To demonstrate the procedure, a flowchart illustrating the stepwise procedure is illustrated in Fig. 8c. In general, the proposed MNSP may be used to quantify the seismic demands of a steel MRF equipped with SSWs progressing to various yielding stages, and the method also retains the advances of the MPA procedure. Concurrently, the MNSP also integrates the inherent advantage of an energy-based procedure [38, 39].

4. Application of the MNSP and discussions

4.1. Prototype steel MRFs with SSWs and ground motions

The proposed MNSP was applied to two prototype steel MRFs equipped with SSWs, and the effectiveness of the procedure for prescribing the peak seismic demands of the system was examined. The prototype buildings were preliminarily designed based on Chinese Code for Seismic Design of Buildings (GB 50011-2010) [41], and the seismic intensity of 9 was assumed (i.e. The basic acceleration was 0.4 gal). To ensure a wide deformation range of the damage-control stage, the steel MRF was designed with the steel of the grade Q460 (yield strength of 460 MPa) [3, 36] for the two structures, and the SSWs were designed with the steel of the grade Q235 (yield strength of 235 MPa). The detailed information about the section of the prototype structures is provided in Table 1. In the table, m and n denote the number of rows of flexural links in the SSW and the number of flexural links in a row, respectively. The width and length of links are denoted by b and h, respectively (unit mm). The thickness of the SSW is represented by t (unit mm). In addition, it was assumed that effective buckling restrained configurations were used. The modal properties of the prototype structures are given in Table 2, and the structural arrangements of the two structures are illustrated in **Appendix B.**

Two ensembles of earthquake ground motion records [1, 42] were used to verify the effectiveness of the proposed MNSP. These earthquake motions were developed by Somerville et al. [42] in the SAC project. The first ensemble of ground motions (i.e. record code LA01-LA20) was for representation of the design basis earthquakes, and the latter

330 (i.e. record code LA21-LA40) was for characterising the maximum considered
331 earthquakes. Both ground motion ensembles correspond to the site condition of stiff soil.
332 The pseudo-acceleration spectra of the earthquake ground motions corresponding to a
333 damping ratio of 5% are shown in Fig. 9.
334
335 *4.2. Analysis description and the responses statistics*

336 In this research, the responses of the prototype structures were determined by the
337 proposed MNSP, and three vibration modes were considered to account for contributions
338 of multi-modes. For the purpose of comparison, pushover analyses with the lateral load
339 distribution documented in FEMA-356 [27] were also performed. It is noted that for the
340 two prototype structures, they might be multi-mode-sensitive according to the modal
341 property information shown in Table 2. Thus, in practical cases, it is required that linear
342 dynamic analysis should also be performed when conducting the nonlinear static procedure
343 in FEMA-356 [27]. Nonetheless, the results from the static procedure can provide an
344 insight into the applicability of the method for prescribing the seismic demand of a steel
345 MRF equipped with SSWs. In particular, the uniform lateral load distribution and the
346 counterpart corresponding to the fundamental vibration mode were used. It is worth
347 mentioning that when applying the procedure of FEMA-356, the 'target displacement' was
348 not estimated by design equations in the provision, but was taken to be identical to that
349 determined by the MNSP (i.e. Section 3). Thus, the comparison was more instructive as
350 the difference between the results by MNSP and the method in FEMA-356 was caused by
351 the lateral load distributions. In both nonlinear static procedures, the gravity load was
352 applied first, and the P-delta effect was included in the analysis. Nonlinear response

353 history analyses (NL-RHAs) of the prototype structures subjected to forty ground motions
354 were also performed. The damping ratio of 5% for the first two vibration modes was
355 assumed for developing the Rayleigh damping matrix. It is worth mentioning that the
356 damping ratio ranging from 2% to 5% may be applicable to steel structures [1, 9, 11, 32],
357 and a significant damping ratio may be used to quantify the damping effect of non-
358 structural elements. Nonetheless, the MNSP also provides sufficient flexibility for
359 practitioners using various damping ratios in practical cases.

360 The pushover responses of the fundamental vibration mode and the roof displacement
361 determined by NL-RHAs are given in Fig. 10, and the base shear force (V) was normalised
362 by the ultimate base shear (V_u). As can be seen, the typical trilinear behaviour was evident,
363 and the two prototype structures progressed to different yielding stages when subjected to
364 the two ground motion ensembles. It is worth pointing out that the maximum interstorey
365 drift of the two structures under the two ground motion database was below 6% which is
366 generally defined as the drift limit of collapse prevention for steel MRFs in FEMA-350
367 [43]. Therefore, it was assumed that all the data points are valid and collapse would not
368 occur for the two structures. However, a reader may be aware that a full-fledged seismic
369 design of the structure also requires quantification of the 'capacity' of the system, which is
370 beyond the scope of the current study.

371 As the roof displacement and the interstorey drift are directly related to structural
372 damage, these demand quantities were explored in detail. Specifically, δ_{MNSP} represents the
373 roof displacement demand by the MNSP, and $\delta_{NL\text{-}RHA}$ represents the counterpart obtained
374 by NL-RHA. The 'exact' peak interstorey drift demand determined by NL-RHA is denoted

375 by $\Delta_{\text{NL-RHA}}$, and the estimated interstorey drift demands determined from MNSP and
376 FEMA-356 are denoted by Δ_{MNSP} and Δ_{FEMA}, respectively.

377 The ability of the static procedures for prescribing the seismic demands of steel MRFs
378 equipped with SSWs was quantified by the ratio of the estimated responses to the 'exact'
379 responses by NL-RHAs. Thus, a roof displacement ratio (δ^*_{MNSP}) and two interstorey drift
380 ratios (i.e. Δ^*_{MNSP} and Δ^*_{FEMA}) were defined, as given by

381 $$\delta^*_{\text{MNSP}} = \frac{\delta_{\text{MNSP}}}{\delta_{\text{NL-RHA}}} \tag{9}$$

382 $$\Delta^*_{\text{MNSP}} = \frac{\Delta_{\text{MNSP}}}{\Delta_{\text{NL-RHA}}} \tag{10}$$

383 $$\Delta^*_{\text{FEMA}} = \frac{\Delta_{\text{FEMA}}}{\Delta_{\text{NL-RHA}}} \tag{11}$$

384 The median response quantity defined by the geometric mean (exponential of the
385 average of the natural log values) was used to evaluate the demands of the systems under
386 an ensemble of ground motions, as given by

387 $$x_{\text{m}} = \exp[\frac{1}{n}\sum_{i=1}^{n}\ln x_i] \tag{12}$$

388 where x_{m}, x_{i} and n are the demand in terms of median value, the demand quantity of a
389 system under an individual ground motion and the number of ground motions (i.e. n=20).
390 The dispersion index (ε) was defined by

391 $$\varepsilon = [\frac{1}{n-1}\sum_{i=1}^{n}(\ln x_i - \ln x_{\text{m}})^2]^{0.5} \tag{13}$$

392 Note that these two statistical indices were demonstrated to be logical for estimating the
393 seismic demands of structures, and they have been used in extensive studies [37, 44].

394

395 *4.3. Roof displacement demands*

396 Fig. 11 presents the roof displacement determined from the MNSP and NL-RHAs. The
397 median roof displacement ratios and the corresponding dispersion measure are also
398 indicated in the figure. For both prototype structures, the results show that the MNSP
399 generally overestimated the roof displacement demand slightly, and the reasonable
400 dispersion was achieved, echoed by the observation that data points were clustered at the
401 forty-five degree diagonal line. With respect to the effect of the ground motion intensity,
402 the analysis data indicate that the accuracy of approximate procedures might deteriorate in
403 case of stronger ground motions, as the median and the dispersion measure of roof
404 displacement ratio both increased with the intensity of ground motions increasing. This
405 observation was reasonable as the coupling effect among multi-vibration modes which was
406 excluded from the MNSP may be more evident when a structure develops significant
407 yielding.

408

409 *4.4. Interstorey drift demands*

410 Fig. 12 presents the interstorey drift demands (median interstorey drift ratios, median
411 interstorey drifts and dispersion measures) of the 5-storey structure. It is seen that the
412 median interstorey drift ratios determined by the MNSP were close to unity when the
413 system was subjected to design-level earthquakes (i.e. LA01-LA20). With the intensity of
414 the ground motion increasing, it was observed that the accuracy of the MNSP deteriorated
415 as the interstorey drift ratio of the structure evidently increased. It was also observed that
416 the median interstorey drift demand predicted by the MNSP agreed well with that from the

417 FEMA-356 method with the fundamental-mode lateral load distribution regardless of the
418 intensity of the ground motions, suggesting that higher modes did not have an appreciable
419 contribution to the seismic demands of the system in this case. Comparatively, the uniform
420 lateral load distribution produced conservative estimates of the median interstorey drift
421 demands at lower storeys, but the counterparts in upper storeys were underestimated. This
422 trend was more evident when the system experienced more intense earthquakes. The
423 dispersion measure of the interstorey drift ratios over the structural height fell in a
424 reasonable range, and the scatteration of the estimates of the MNSP was generally smaller
425 than that by the FEMA-356, particularly in upper storeys.

426 Fig. 13 illustrates the corresponding interstorey drift demands of the 10-storey prototype
427 structure subjected to the seismic excitations. In general, the MNSP resulted in satisfactory
428 estimates of the interstorey drift demand ratios, while relatively more pronounced
429 inconsistency between the predictions by the MNSP and NL-RHAs was observed when
430 the structure was subjected to more intense seismic events (i.e. LA21-LA40). Nonetheless,
431 the MNSP generally produced conservative estimates of the median interstorey drift
432 demand, as shown in Fig. 13. This observation echoed the trend of the predicted roof
433 displacement demands and may be induced by the more evident coupling effect arising
434 from multi-modes under intense earthquake events. In contrast, for the predictions by the
435 lateral load distribution of the fundamental vibration mode in FEMA-356, the results in
436 Fig. 13 suggested that the median interstorey drift demand at upper storeys was
437 underestimated when the structure experienced the design-level seismic events (i.e. LA01-
438 LA20), and this trend was aggravated when the structure experienced more intense

439 excitations. This finding was not surprising as the contribution of higher vibration mode
440 became more significant when inelasticity of the structure was sufficiently developed
441 under more intense excitations (i.e. LA21-LA40). As for the uniform lateral load
442 distribution, the similar phenomenon as observed in the 5-storey structure was seen.

443 In practical engineering, to verify the adequacy of a design strategy or to evaluate an
444 existing structure, building codes generally specify a maximum interstorey drift as a
445 threshold [45]. In this context, it is instructive to compare the maximum interstorey drift
446 demand over all stories determined from the MNSP and the NL-RHA to examine the
447 practical effectiveness of the MNSP. Fig. 14 presents the maximum interstorey drift
448 demands over all stories determined by NL-RHAs and the counterparts by the MNSPs as
449 abscissa and ordinate, respectively. As can be seen, the MNSP led to reasonable estimates
450 of the median demands and the corresponding dispersion fell in an acceptable range.
451 Importantly, the accuracy of the MNSP for quantifying the maximum interstorey drift
452 demand did not evidently deteriorate when systems were subjected to more intense
453 earthquakes, demonstrating its potential for practical applications.

454

455 *4.5. Further discussions and comments*

456 A key element of the MNSP is the quantification of the energy factor of the modal
457 oscillators representing an influential mode of a steel MRF equipped with SSWs. Thus,
458 sensitivity analyses of the energy factor were performed using the modal oscillators with
459 varied hysteretic parameters to shed lights on the effect of multi-yielding stages on the
460 seismic demands of the system, and the focus was given to the ultimate stage of a system.
461 A companion work [35] showed that the energy factor is not sensitive to the post-yielding

462 stiffness ratio of the ultimate stage (i.e. α_2) for a trilinear oscillator. Thus, α_2 of the ultimate
463 stage was assumed to be zero for simplification.

464 Representative mean energy factors of oscillators with various hysteretic parameters
465 subjected to ground motions LA01-LA20 are given in Fig. 15, and the oscillators had the
466 identical elastic period to the modal oscillators representing the prototype structures. As a
467 general remark, the energy factor of an oscillator was appreciably influenced by the
468 parameters characterising the multi-yielding stages, but the effect was period-dependent.
469 The energy factor of the oscillator with the period of the fundamental mode of the 5-storey
470 structure increased with increasing post-yielding stiffness ratio of the damage-control stage
471 (i.e. α_1). Comparatively, the reversed trend was characterised for the modal oscillator
472 representing the higher mode of the system. For the oscillator representing the 10-storey
473 structure, positive correlation was characterised among the energy factor, α_1 and ζ_1 for the
474 two vibration modes. It was also observed that the energy factor evidently increased with
475 increasing ductility for short-period modal oscillators (e.g. second mode for the 5-storey
476 structure and 10-storey structure), exhibiting the phenomenon of 'energy lock' [40]. In
477 practical engineering, the seismic demand of a steel MRF equipped with SSWs can be
478 readily modulated by adjusting structural design strategy, and this research work just puts
479 forth a promising tool for quantifying the effect of the influential parameters.

480 However, it is re-emphasised that some trade-offs were made between the theoretical
481 rigorousness and the practical simplicity when developing the MNSP, as reflected by the
482 adopted assumptions in Section 3. Thus, it is also of significance to point out the
483 limitations of both nonlinear static procedures and energy-based methods. For instance, the

484 'reversal' of the pushover response may be observed when implementing the modal
485 pushover analysis (MPA) procedure [25, 38]. The recently expanded energy-balance-based
486 seismic design methodology was generally developed based on energy balance of
487 equivalent oscillators, and hence empirical expressions of the lateral force distributions
488 over the structure [46-48] may not replicate realistic lateral force pattern under earthquake
489 motions. To combat the drawbacks produced by these methods, the proposed MNSP
490 procedure was built on the framework of the MPA procedure [25, 38], and the energy
491 factor was only used to determine the target displacement for a trilinear modal oscillator.
492 In this context, the effectiveness of the MNSP would not be further undermined when the
493 energy concept is utilised carefully, which is in line with recent research findings [32, 39].
494 However, the accuracy of MNSP can be evidently compromised in the cases of torsion-
495 sensitive structures [49] and structures with strength and stiffness irregularity [50]. In
496 addition, although the MPA-based procedures may overcome some limitations of
497 conventional nonlinear static procedures [24, 51, 52] and provide a physical basis towards
498 a deeper understanding of the cascading effect of the hysteretic parameters and earthquake
499 motion characteristics on the seismic responses of inelastic systems, ignoring the coupling
500 effect among multi-vibration modes may produce inconsistent estimates of the seismic
501 demands. Thus, the MNSP is not recommended for quantifying the seismic demand of a
502 structure subjected to a single earthquake ground motion, echoed by interstorey drift ratio
503 demands under individual ground motions as given in Fig. 12 and Fig. 13. In summary, a
504 reader should be aware that although the proposed MNSP shows satisfactory accuracy for
505 quantifying the seismic demand of a steel MRF equipped with SSWs showing multiple

yielding stages based on an ensemble of earthquake ground motions, the adequacy of the MNSP should be complemented by the NL-RHA in seismic design and evaluations.

5. Conclusions

The current study focuses on a multi-stage-based nonlinear static procedure (MNSP) for quantifying the seismic demands of steel moment resisting frames (MRFs) equipped with steel slit walls (SSWs). The paper commenced with clarification of the hysteretic behaviour of steel MRFs equipped with SSWs exhibiting multi-yielding stages, and recent experimental findings were also revisited. An effective finite element model for replicating the cyclic response of a steel MRF equipped with SSWs was proposed and verified by the test data. The MNSP motivated by energy balance concept was then introduced using the concept of modal single-degree-of-freedom (SDOF) systems, and the effectiveness of the method was demonstrated based on prototype structures subjected to forty ground motions. The main research findings drawn from this work are presented as follows:

1. The hysteretic behaviour of a steel MRF equipped with SSWs may alter in different yielding stages. When buckling of SSWs is avoided, the hysteretic force-displacement response of a steel MRF equipped with SSWs showing multi-yielding stages can be idealised by a trilinear kinematic model.
2. The proposed MNSP procedure produced satisfactory estimates of the peak seismic demands (i.e. the roof displacement demand, the interstorey drift demand and the interstorey drift demand over all storeys) of prototype steel MRFs equipped with

SSWs. In contrast, inconsistent estimates of seismic demands were obtained by the fundamental vibration mode lateral load distribution and the uniform load distribution recommended by FEMA-356, particularly in cases where the contribution of higher vibration mode was pronounced.

3. The comparative study of prototype structures subjected to two ensembles ground motions representing design basis earthquakes and maximum considered earthquakes shows that the accuracy of the MNSP may deteriorate slightly with ground motion intensity increasing, but generally conservative results can be obtained.

4. The seismic demand of a steel MRF equipped with SSWs is appreciably influenced by the multi-yielding stages of the system. As a dual system, the influential hysteretic parameters can be adjusted flexibly by modulating the structural design strategy, and an optimised design can also be achieved using the MNSP in the design phase.

Despite the reasonable predictions produced by the MNSP, it should be re-emphasised that the theoretical rigorousness of the MNSP is compromised compared with the NL-RHA due to the nature of a simplified method. Ignoring the coupling effect among the modal coordinates in the nonlinear stage accompanied by simple modal combination may result in inconsistent estimates of seismic demands of steel MRFs equipped with SSWs when the MNSP is applied to quantifying seismic demands of a structure subjected to a single seismic event. Thus, the adequacy of the MNSP should be verified by NL-RHA when finalising the seismic design and evaluation of a steel MRF equipped with SSWs. In

addition, although the present study focuses on the peak response demands, the MNSP can be extended to multi-demand indices accounting for the cumulative demand of the system, and this work is currently being conducted by the authors.

Acknowledgements

This work is financially supported by the National Key Research and Development Program of China (Grant No. 2016YFC0701202) and National Natural Science Foundation of China (Grant No. 51890902). Partial funding supports received from the Chinese National Engineering Research Centre for Steel Connection, The Hong Kong Polytechnic University (Project No. 1-BBYQ) are also acknowledged. The fifth author would also like to acknowledge the funding support by Science and Technology Innovative Research Team Project of Universities in Hunan Province (Grant No. 2015-616).

Appendix A

The detailed procedure for developing the capacity curve of an energy-based modal oscillator can be found in [38, 40], and it is reproduced herein for clarity. In particular, the energy absorbed by a modal oscillator is identical to the external work done by the invariant lateral load, given by

$$\delta W_n^m = \frac{1}{2}(\mathbf{L}_n^{m-1} + \mathbf{L}_n^m)\cdot(\mathbf{U}_n^m - \mathbf{U}_n^{m-1}) \tag{A.1}$$

where δW_{n}^m = incremental external work at the m^{th} step for the n^{th} mode and $\mathbf{U}_{\mathrm{n}}$ = the lateral deformation profile of floors subjected to the lateral load pattern of the n^{th} mode.

572 Therefore, the quantity defined as the energy-based displacement ($u_{e,n}$) of the oscillator
573 for the n^{th} mode may be extracted, as reproduced in Fig. A1. The energy-based
574 displacement in the incremental form [38, 40] is expressed by

575 $$\delta u_{e,n}^{m} = \frac{\delta W_n^m}{\frac{1}{2}(V_n^m + V_n^{m-1})} \tag{A.2}$$

576 where $\boldsymbol{V}_n$ = the base shear force corresponding to the $\boldsymbol{n}^{th}$ mode, which is reproduced by

577 $$V_n^m = \mathbf{L}_n^m \cdot \mathbf{1} \tag{A.3}$$

578 Therefore, the capacity curve representing the $\boldsymbol{n}^{th}$ mode is reproduced and given by

579 $$W_n^m = W_n^{m-1} + \delta W_n^m \tag{A.4}$$

580 $$u_{e,n}^{m} = u_{e,n}^{m-1} + \delta u_{e,n}^{m} \tag{A.5}$$

581 A simplified method for idealising the pushover curves response with a multi-linear
582 approximation was proposed by Ke and Chen [3], and the detail is also reproduced herein
583 for clarity. Specifically, the data extracted from the base shear force versus energy-based
584 displacement response curve for all essential modes are firstly normalised by

585 $$\iota = \frac{u_{e,n}}{u_{max,n}} \tag{A.6}$$

586 $$\omega = \frac{V_n}{V_{max,n}} \tag{A.7}$$

587 where $u_{max,n}$ = maximum energy-based displacement for the n^{th} mode (preselected in a
588 pushover analysis); $V_{max,n}$ = maximum force. Based on the assumption of the trilinear
589 approximation, the idealised curve for n^{th} mode can be expressed as

590 $$\omega = \begin{cases} k_n \iota & 0 \le \iota \le \iota_1 \\ \alpha_{1,n} k_n \iota + (1-\alpha_{1,n}) k_n \iota_1 & \iota_1 < \iota \le \iota_2 \\ \alpha_{1,n} k_n \iota + (\alpha_{1,n} - \alpha_{2,n}) k_n \iota_2 + (1-\alpha_{1,n}) k_n \iota_1 & \iota_2 < \iota \le 1 \end{cases} \tag{A.8}$$

where k_n = initial stiffness of the normalised idealised curve for the n^{th} mode; ι_1 = displacement characterising yielding of SSWs in the idealised curve (Fig. A2); ι_2 = displacement characterising yielding of the MRF in the idealised curve (Fig. A2); $\alpha_{1,n}$ = post-yielding stiffness ratio of the damage-control stage for the n^{th} mode and $\alpha_{2,n}$ = post-yielding stiffness ratio of the ultimate stage for the n^{th} mode. Utilising the least-square principle, the governing function [3] is expressed as

$$G = \sum_{i=1}^{M} (k_n \iota_i - \omega_i)^2 + \sum_{i=M+1}^{M+N} [\alpha_{1,n} k_n (\iota_i - \iota_1) + k_n \iota_1 - \omega_i)]^2 + \sum_{i=M+N+1}^{M+N+Q} [\alpha_{2,n} k_n (\iota_i - \iota_2) + \alpha_{1,n} k_n (\iota_2 - \iota_1) + k_n \iota_1 - \omega_i)]^2 \quad \text{(A.9)}$$

where M = number of data points in the phase where a steel MRF equipped with SSWs responds elastically; N = number of data points in the damage-control stage in which inelastic actions are generally locked in SSWs and Q = number of data points in the phase where all members of the system develop significant yielding. Therefore, the hysteretic parameters of the trilinear idealisation can be finalised if the target function reached the minimum.

Appendix B

The detailed geometric information about the arrangement of the prototype structures is schematically shown in Fig. B1.

References

[1] Erochko J, Christopoulos C, Tremblay R, Choi H. Residual drift response of SMRFs and BRB frames in steel buildings Designed according to ASCE 7-05. J Struct Eng

2011; 137(5): 589-599.

[2] Baiguera M, Vasdravellis G, Karavasilis TL. Dual seismic-resistant steel frame with high post-yield stiffness energy-dissipative braces for residual drift reduction. J Constr Steel Res 2016;122:198-212.

[3] Ke K, Chen Y. Seismic performance of MRFs with high strength steel main frames and EDBs. J Constr Steel Res 2016; 126: 214-228.

[4] Pampanin S, Christopoulos C, Nigel Priestley MJ. Performance-based seismic response of frame structures including residual deformations part II: multi-degree of freedom systems. J Earthq Eng 2003;7(1):119-147.

[5] Christopoulos C, Pampanin S, Nigel Priestley MJ. Performance-based seismic response of frame structures including residual deformations part I: single-degree of freedom systems. J Earthq Eng 2003;7(1):97-118.

[6] Bruneau M, Chang SE, Eguchi RT, Lee GC, O'Rourke TD, Reinhorn A, Von Winterfeldt D. A framework to quantitatively assess and enhance the seismic resilience of communities. Earthq spectra 2003; 19(4): 733-752.

[7] Cimellaro GP, Reinhorn A, Bruneau M. Framework for analytical qualification of disaster resilience. Eng Struct 2010; 32(11): 3639-3649.

[8] Guo JWW, Christopoulos C. Performance spectra based method for the seismic design of structures equipped with passive supplemental damping systems. Earthq Eng Struct Dyn 2013; 42(6): 935-952.

[9] Vargas R, Bruneau M. Analytical response and design of buildings with metallic Structural Fuses. I. J Struct Eng 2009; 135(4): 386-393.

[10] Connor JJ, Wada A, Iwata M, Huang YH. Damage-controlled structures. I: Preliminary design methodology for seismically active regions. J Struct Eng 1997; 123(4): 423-431.

[11] Vargas R, Bruneau M. Experimental response of buildings designed with metallic structural fuses. II. J Struct Eng 2009; 135(4): 394-403.

[12] Dubina D, Dinu F. Experimental evaluation of dual frame structures with thin-walled steel panels. Thin-Walled Struct 2014; 78(4): 57-69.

[13] Chen SJ, Jhang C. Cyclic behavior of low yield point steel shear walls. Thin-Walled Struct 2006; 44(7): 730-738.

[14] Qu B, Bruneau M, Lin CH, Tsai KC. Testing of full-scale two-story steel plate shear wall with reduced beam section connections and composite floors. J Struct Eng 2008; 134(3): 364-373.

[15] Hitaka T, Matsui C. Experimental Study on Steel Shear Wall with Slits. J Struct Eng 2003; 129(5): 586-595.

[16] Hitaka T, Matsui C, Sakai J. Cyclic tests on steel and concrete-filled tube frames with Slit Walls. Earthq Eng Struct Dyn 2007; 36(6): 707-727.

[17] Jacobsen A, Hitaka T, Nakashima M. Online test of building frame with slit-wall dampers capable of condition assessment. J Constr Steel Res 2010; 66(11): 1320-1329.

[18] He L, Togo T, Hayashi K, Kurata M, Nakashima M. Cyclic Behavior of Multirow Slit Shear Walls Made from Low-Yield-Point Steel. J Struct Eng 2016; 142(11): 04016094.

[19] Khatamirad M, Shariatmadar H. Experimental and analytical study of steel slit shear wall. Steel Compos Struct 2017; 24(6): 741-751.

[20] Kim J, Kim M, Eldin MN. Optimal distribution of steel plate slit dampers for seismic retrofit of structures. Steel Compos Struct 2017; 25(4): 473-484.

[21] Cortés G, Liu J. Experimental evaluation of steel slit panelframes for seismic resistance. J Constr Steel Res 2011; 67(2): 181-191.

[22] Ke K, Chen Y. Energy-based damage-control design of steel frames with steel slit walls. Struct Eng Mech 2014; 52(6): 1157-1176.

[23] Wang W, Kong J, Zhang Y, Chu G, Chen Y. Seismic Behavior of Self-Centering Modular Panel with Slit Steel Plate Shear Walls: Experimental Testing. J Struct Eng 2018; 144(1): 04017179.

[24] Krawinkler H, Seneviratna GDPK. Pros and cons of a pushover analysis of seismic evaluation. Eng Struct 1998; 20(4): 452-464.

[25] Chopra AK, Goel RK. A modal pushover analysis procedure for estimating seismic demands for buildings. Earthq Eng Struct Dyn 2002; 31(3): 561-582.

[26] Kalkan E, Kunnath SK. Assessment of current nonlinear static procedures for seismic evaluation of buildings. Eng Struct 2008; 29(3): 305-316.

[27] FEMA. Pre-standard and commentary for the seismic rehabilitation of buildings, FEMA-356, SAC Joint Venture, Federal Emergency Management Agency, Washington, DC. 2000.

[28] ABAQUS Analysis User's Manual. ABAQUS Standard, Version 6.12; 2012.

[29] Cortes G. Steel slit panel frames for lateral resistance of buildings. PhD Dissertation, Purdue University; 2009.

[30] EN 1993-1-9. Eurocode 3: design of steel structural – Part 1–9. Brussels, Belgium: CEN, European Committee for Standardization; 2005.

[31] Housner GW. Limit design of structures to resist earthquakes. Proceeding of the 1st WCEE. 1956.

[32] Leelataviwat S, Saewon W, Goel SC. Application of energy balance concept in seismic evaluation of structures. J Struct Eng 2009; 135(2): 113-121.

[33] Lee SS, Goel SC, Chao SH. Performance-based design of steel moment frames using target drift and yield mechanism. Research Report No. UMCEE 01-17, Department of

Civil and Environmental Engineering, University of Michigan, Ann Arbor, Michigan. 2001.

[34] Ke K, Ke S, Chuan G. The energy factor of systems considering multiple yielding stages during ground motions. Soil Dyn Earthq Eng 2015; 71: 42-48.

[35] Ke K, Zhao Q, Yam MCH, Ke S. Energy factors of trilinear SDOF systems representing damage-control buildings with energy dissipation fuses subjected to near-fault earthquakes. Soil Dyn Earthq Eng 2018; 107: 20–34.

[36] Ke K, Yam MCH. A performance-based damage-control design procedure of hybrid steel MRFs with EDBs. J Constr Steel Res 2018; 143:46-61.

[37] Chopra AK, Goel RK, Chintanapakdee C. Evaluation of a modified MPA procedure assuming higher modes as elastic to estimate seismic demands. Earthq Spectra 2004; 20(3): 757-778.

[38] Hernandez-Montes E, Kwon OS, Aschheim MA. An energy-based formulation for first- and multiple-mode nonlinear static (pushover) analyses. J Earthq Eng 2004; 8(1): 69-88.

[39] Jiang Y, Li G, Yang D. A modified approach of energy balance concept based multimode pushover analysis to estimate seismic demands for buildings. Eng Struct 2010; 32(5): 1272-1283.

[40] Ke K, Yam MCH, Ke S. A dual-energy-demand-indices-based evaluation procedure of damage-control frame structures with energy dissipation fuses. Soil Dyn Earthq Eng 2017; 95: 61-82.

[41] CMC. Code for Seismic Design of Buildings (GB 50011-2010). China Ministry of Construction: Beijing, 2010.

[42] Somerville P. Development of ground motion time histories for phase 2 of the FEMA/SAC steel project, SAC Background Document SAC/BD-91/04. Sacramento,

Calif: SAC Joint Venture, 1997.

[43] FEMA. Recommended seismic design criteria for new steel moment frames buildings, FEMA-350, SAC Joint Venture, Federal Emergency Management Agency, Washington DC. 2000.

[44] Chintanapakdee C, Chopra AK. Evaluation of modal pushover analysis using generic frames. Earthq Eng Struc Dyn 2003; 32(3): 417-442.

[45] Nguyen AH, Chintanapakdee C, Hayashikawa T. Assessment of current nonlinear static procedures for seismic evaluation of BRBF buildings. J Constr Steel Res 2010; 66(8-9): 1118-1127.

[46] Goel SC, Liao WC, Reza Bayat M, Chao SH. Performance-based plastic design (PBPD) method for earthquake-resistant structures: an overview. Struct Des Tall Spec 2010; 19(1-2): 115-137.

[47] Sahoo DR, Chao SH. Performance-based plastic design method for buckling-restrained braced frames. Eng Struct, 2010, 32(9): 2950-2958.

[48] Chao SH, Goel SC, Lee SS. A seismic design lateral force distribution based on inelastic state of structures. Earthq Spectra 2007; 23(3): 547-569.

[49] Chopra AK, Goel RK. A modal pushover analysis procedure to estimate seismic demands for unsymmetric-plan buildings. Earthq Eng Struct Dyn 2004; 33(8): 903-927.

[50] Chopra AK, Chintanapakdee C. Evaluation of modal and FEMA pushover analyses: vertically “regular” and irregular generic frames. Earthq Spectra 2004; 20(1): 255-271.

[51] Antoniou S, Pinho R. Advantages and limitations of adaptive and non-adaptive force-based pushover procedures. J Earthq Eng 2004; 8(04): 497-522.

[52] Kalkan E, Kunnath SK. Adaptive modal combination procedure for nonlinear static analysis of building structures. J Struct Eng 2006; 132(11): 1721-1731.

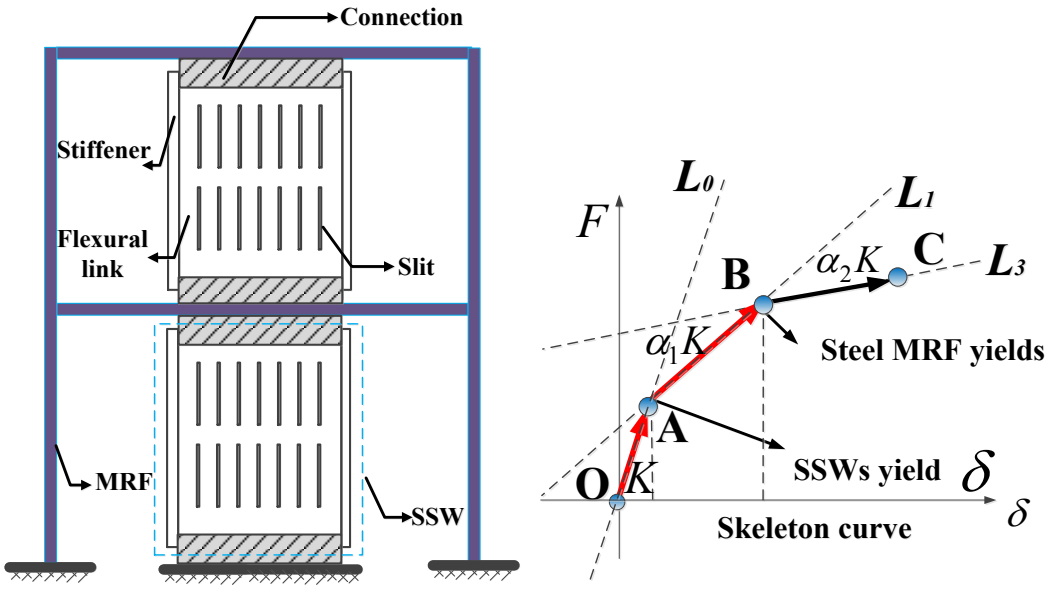

(a) (b)

Fig. 1 Multi-yielding stages of a steel MRF equipped with SSW: (a) concept of steel MRF equipped with SSW and (b) skeleton response.

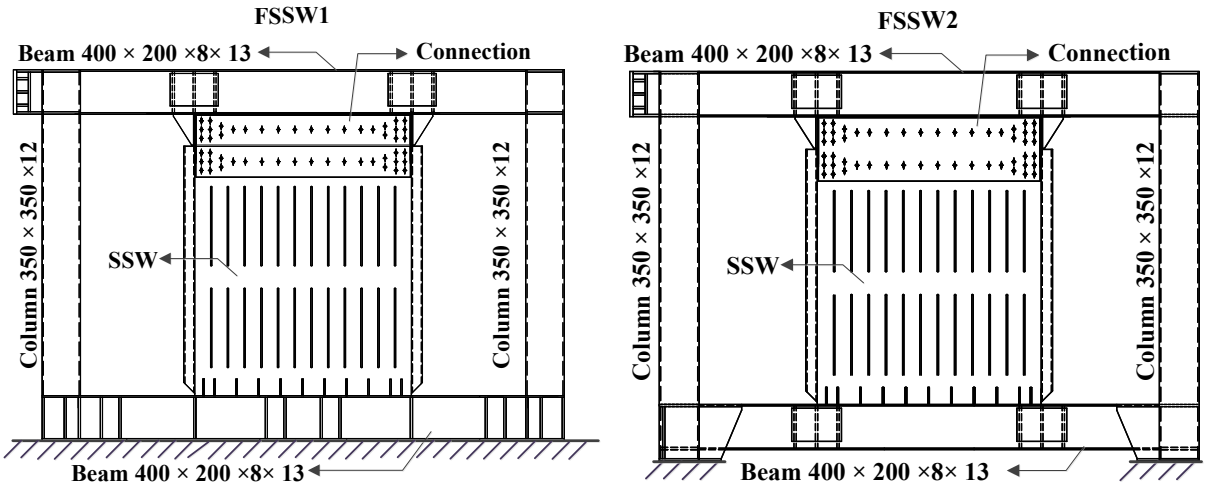

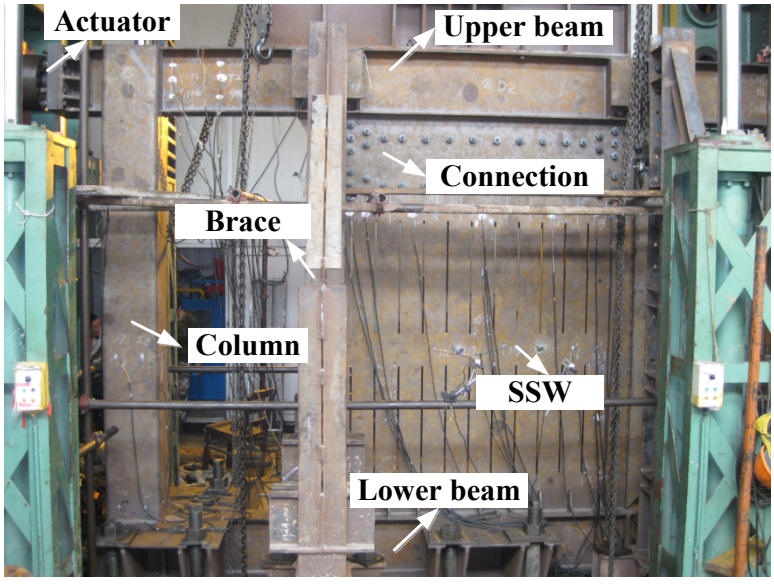

Fig. 2 Specimens of steel MRFs equipped with SSWs [22].

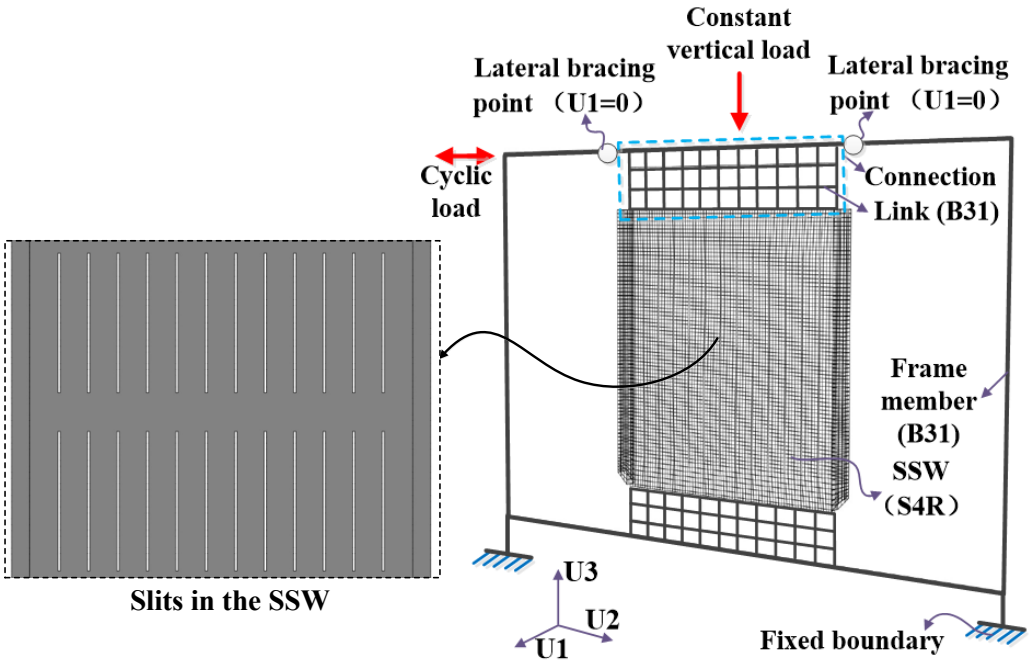

Fig. 3 Overview of numerical models of steel MRFs equipped with SSWs.

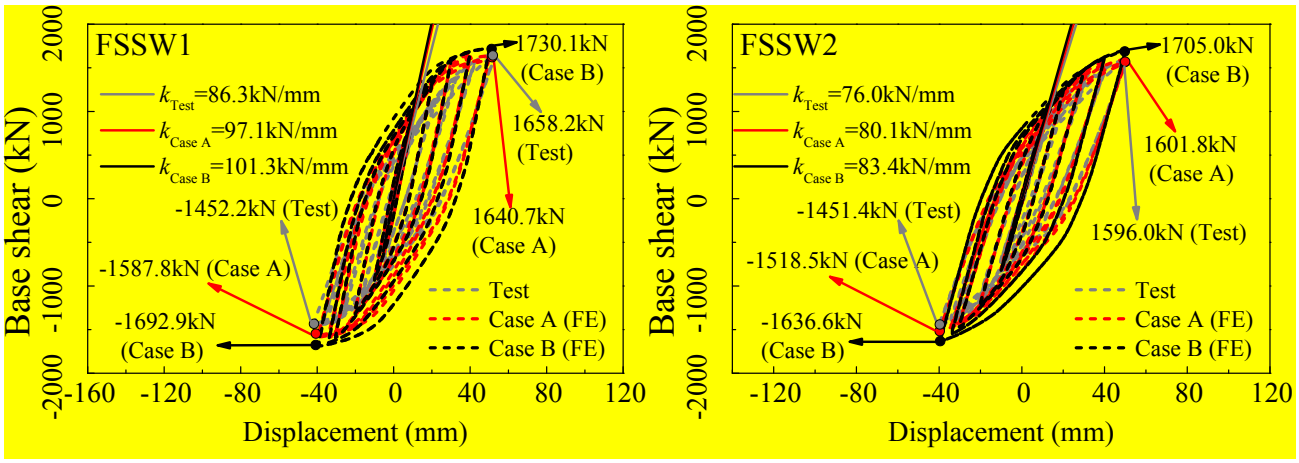

(a) (b)

Fig. 4 Comparison of test results and FE predictions: (a) FSSW1 and (b) FSSW2.

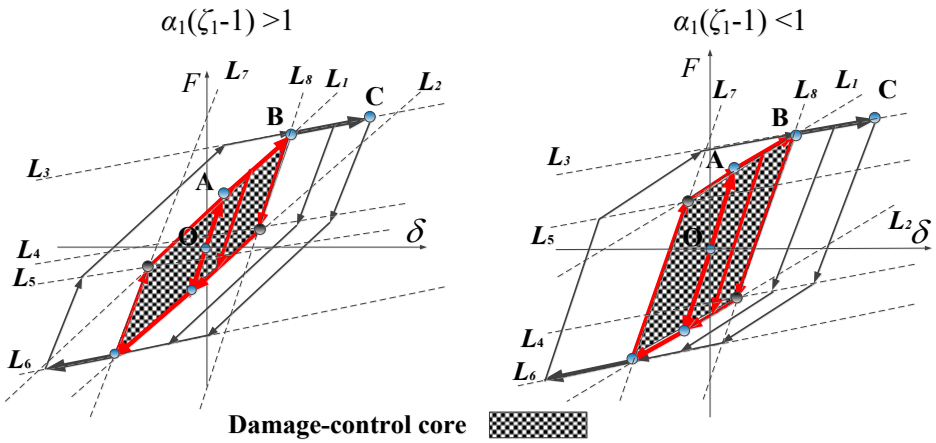

Fig. 5 Hysteretic model.

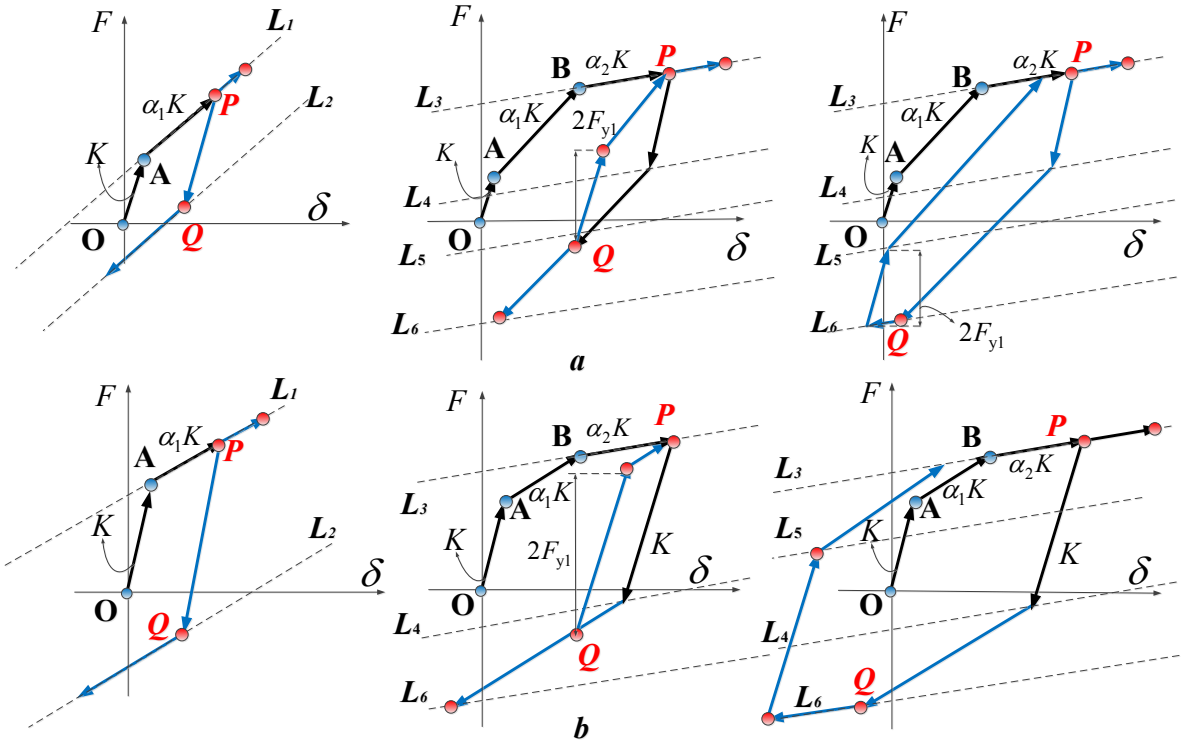

Fig. 6 Hysteretic path of a steel MRF equipped with SSWs: (a) $\alpha_1(\zeta_1\text{-}1) > 1$ and (b) $\alpha_1(\zeta_1\text{-}1) \leq 1$.

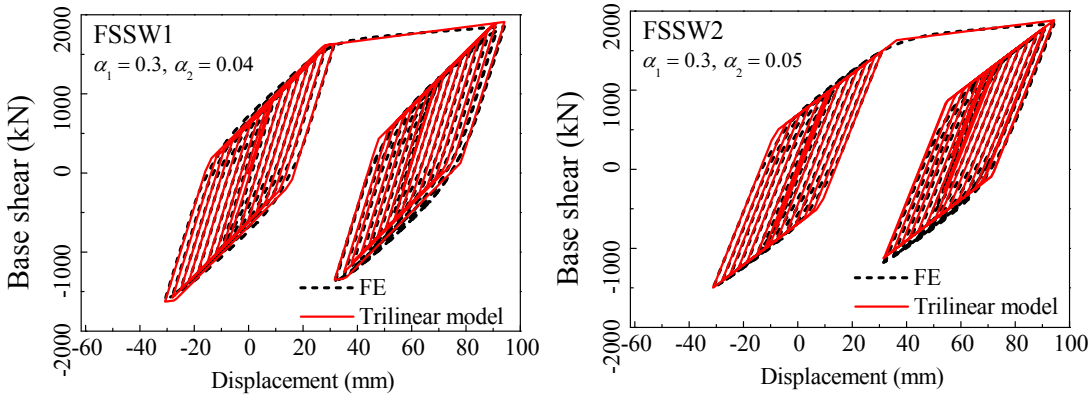

Fig. 7 Shift of the damage control core.

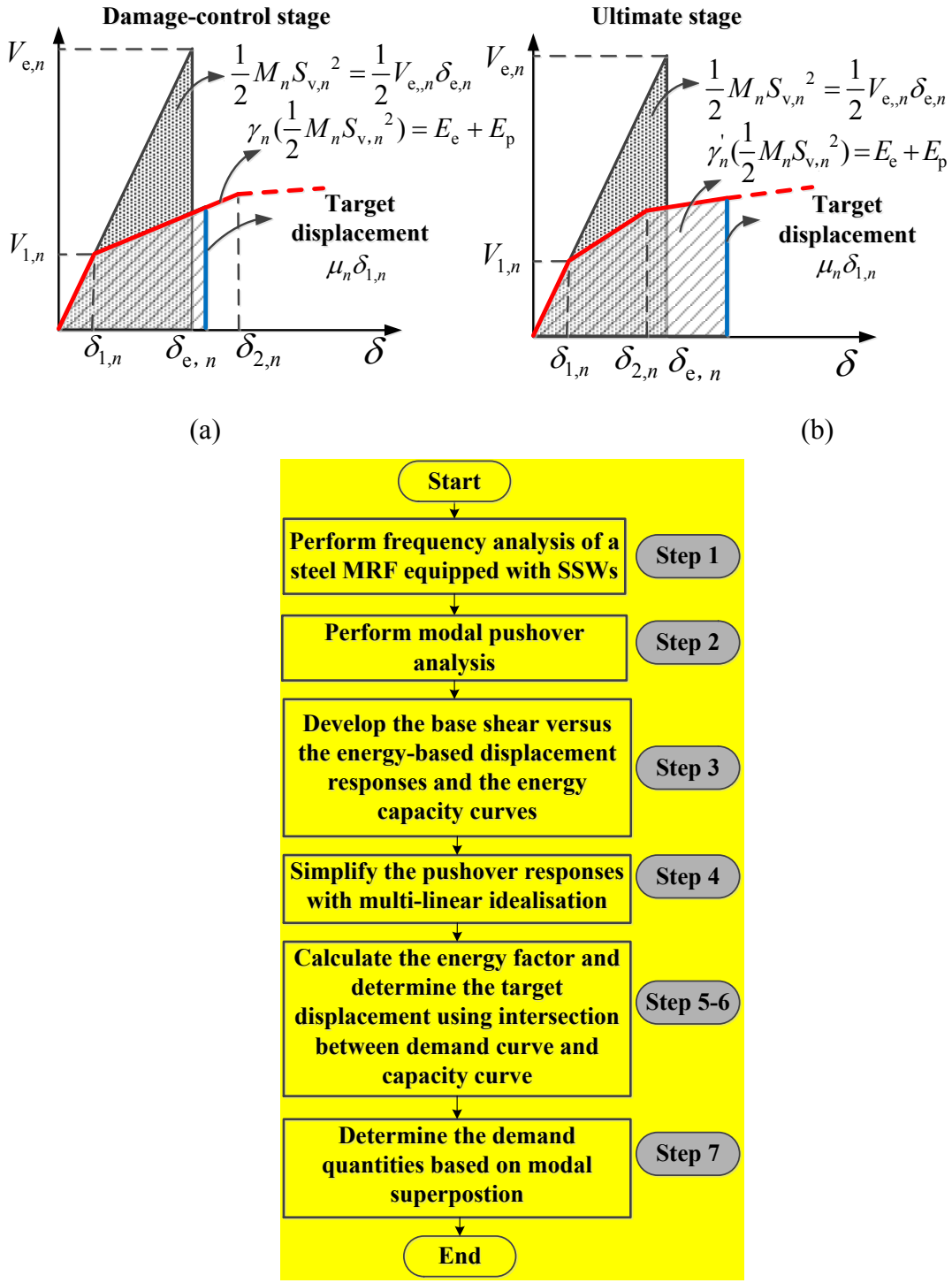

Fig. 8 Energy factor of steel MRFs equipped with SSWs in multi-yielding stages and the MNSP: (a) damage-control stage, (b) ultimate stage and (c) flowchart of the MNSP.

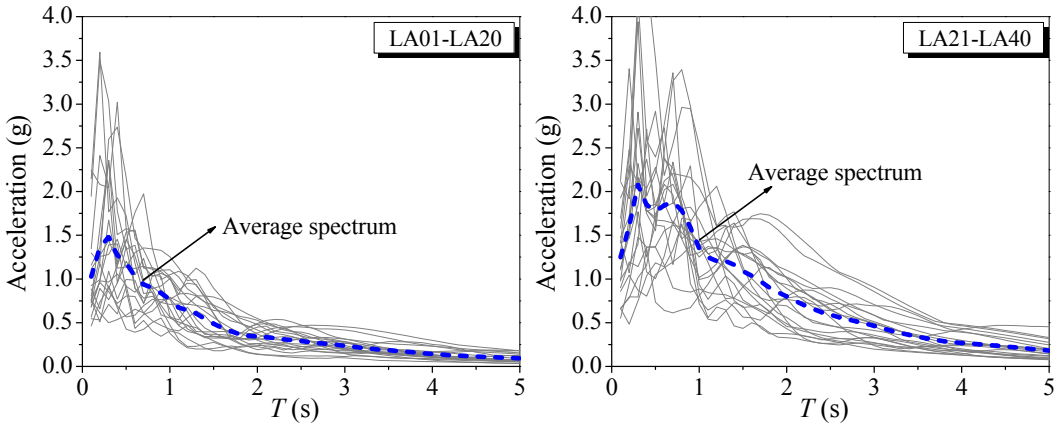

(a) (b)

Fig. 9 Acceleration spectra of the ground motion ensembles: (a) design basis earthquakes and (b) maximum considered earthquakes.

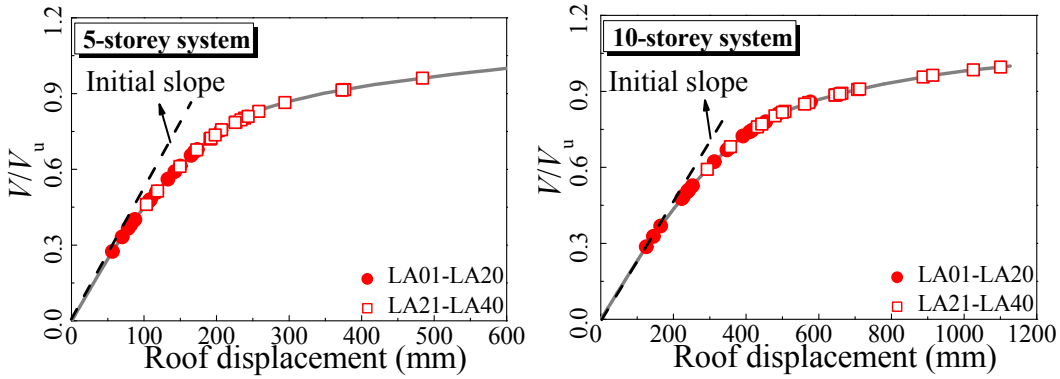

Fig. 10 The first mode pushover curves (the fundamental mode) and roof displacements determined by NL-RHAs.

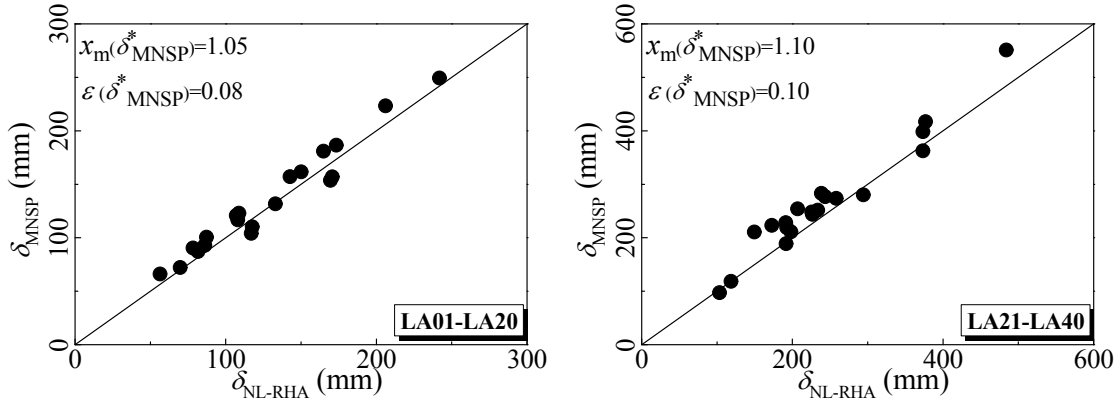

(a)

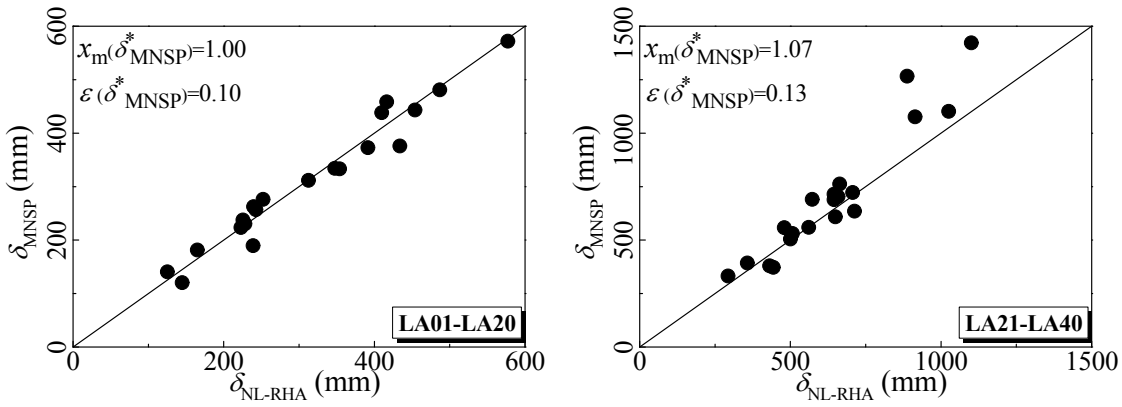

(b)

Fig. 11 Roof displacement demands by different procedures: (a) 5-storey structure and (b) 10-storey structure.

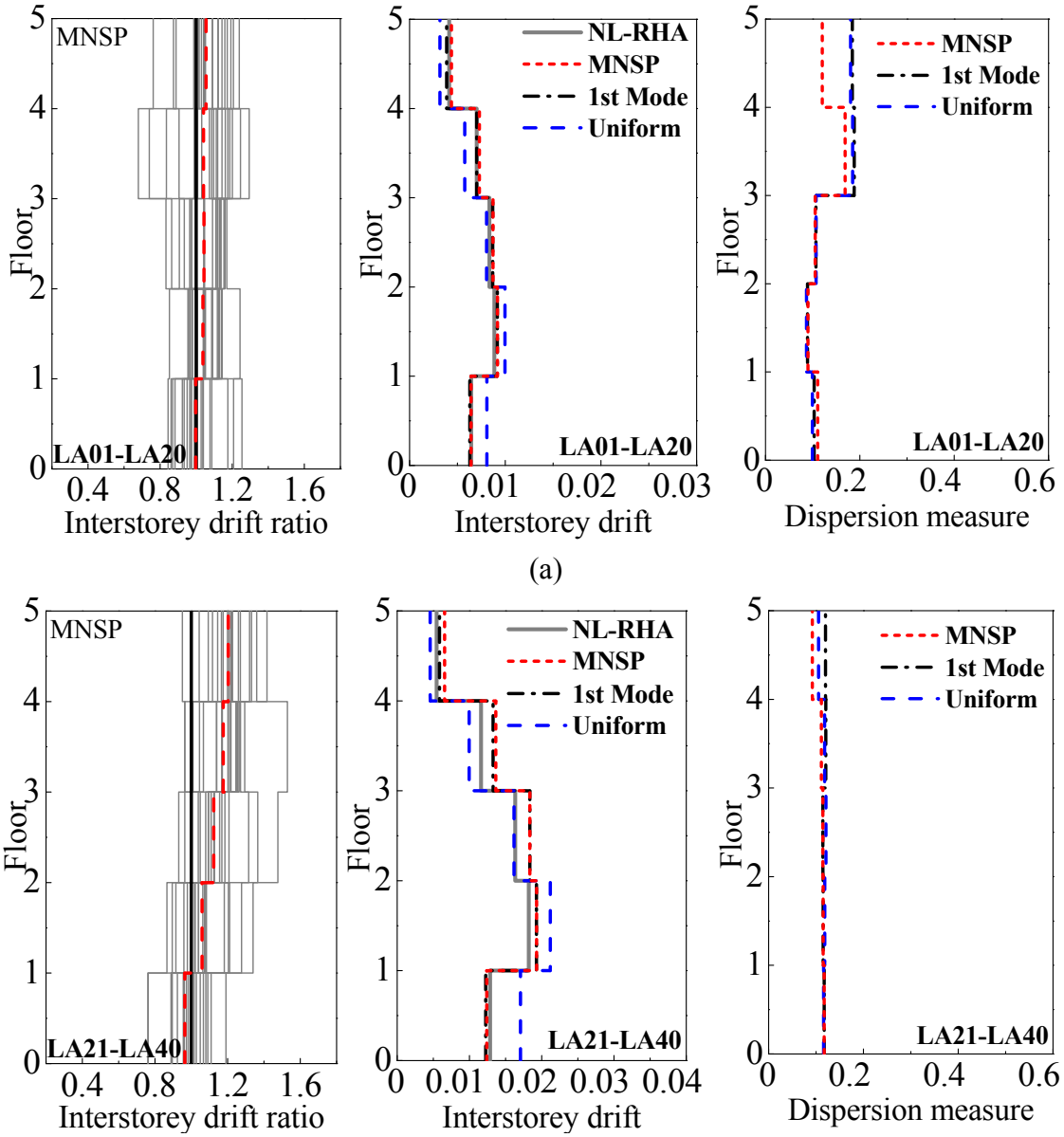

Fig. 12 Interstorey drift demands of the 5-storey structure : (a) under design basis earthquakes (LA01-LA20) and (b) under maximum considered earthquakes (LA21-LA40).

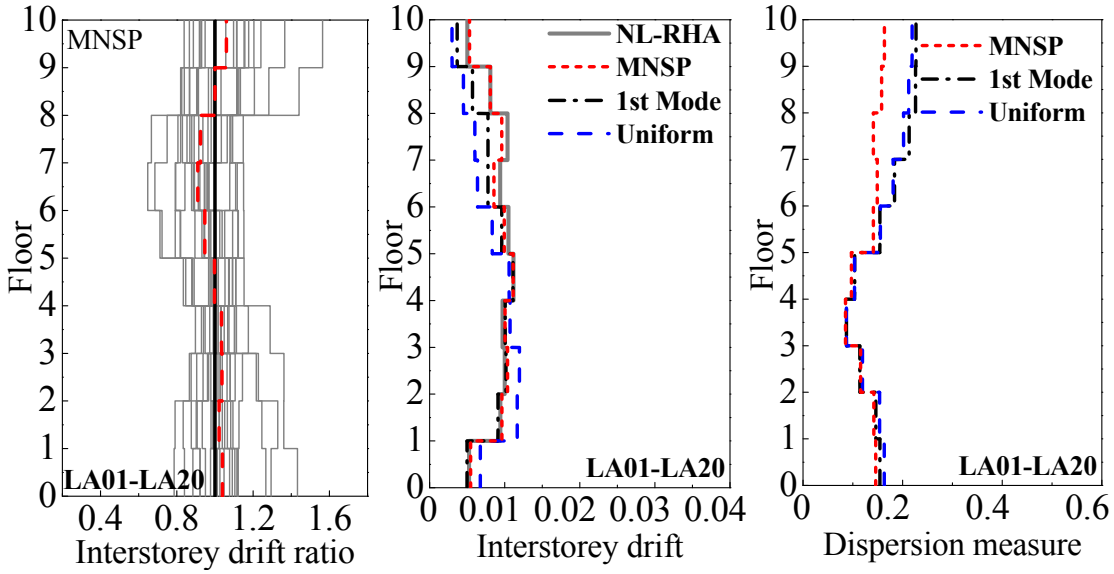

(a)

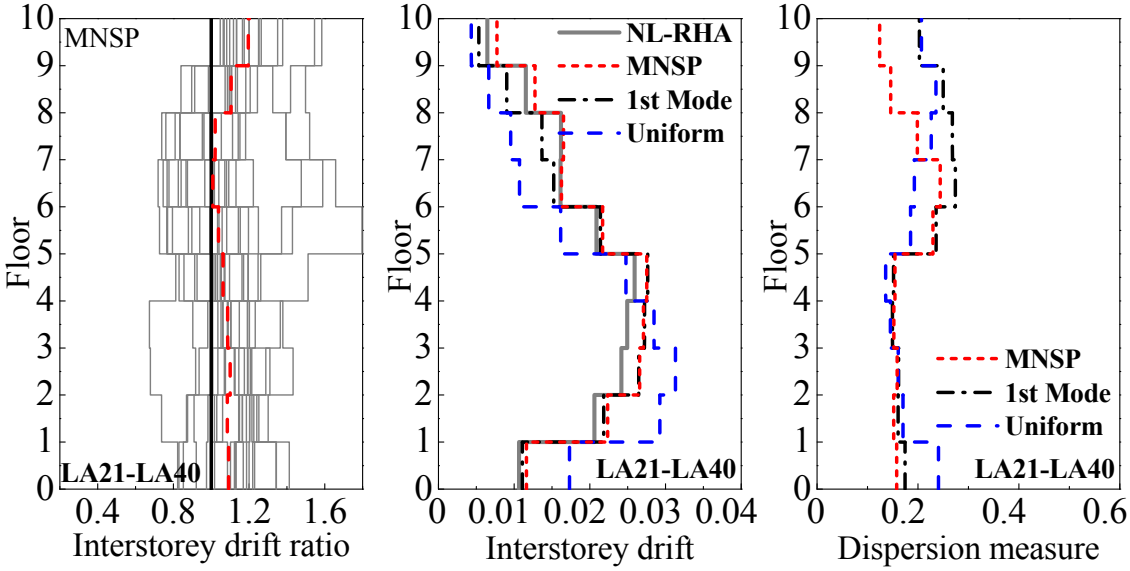

(b)

Fig. 13 Interstorey drift demands of the 10-storey structure: (a) under design basis earthquakes (LA01-LA20) and (b) under maximum considered earthquakes (LA21-LA40).

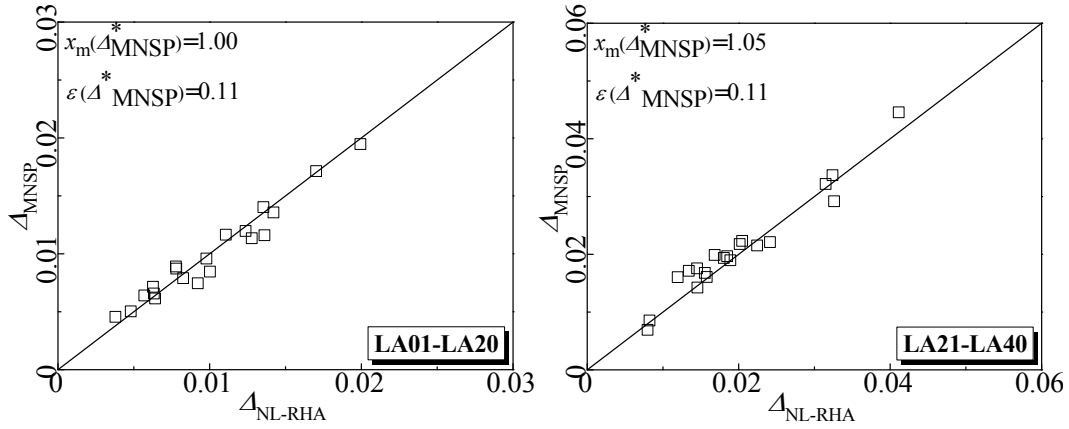

(a)

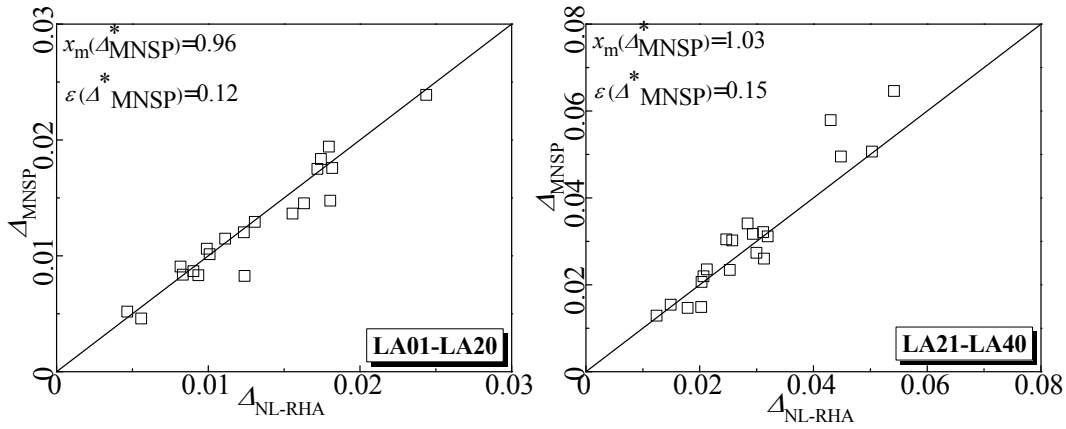

(b)

Fig. 14 Comparison of maximum interstorey drift demands determined from NL-RHA and the MNSP: (a) 5-storey structure and (b) 10-storey structure.

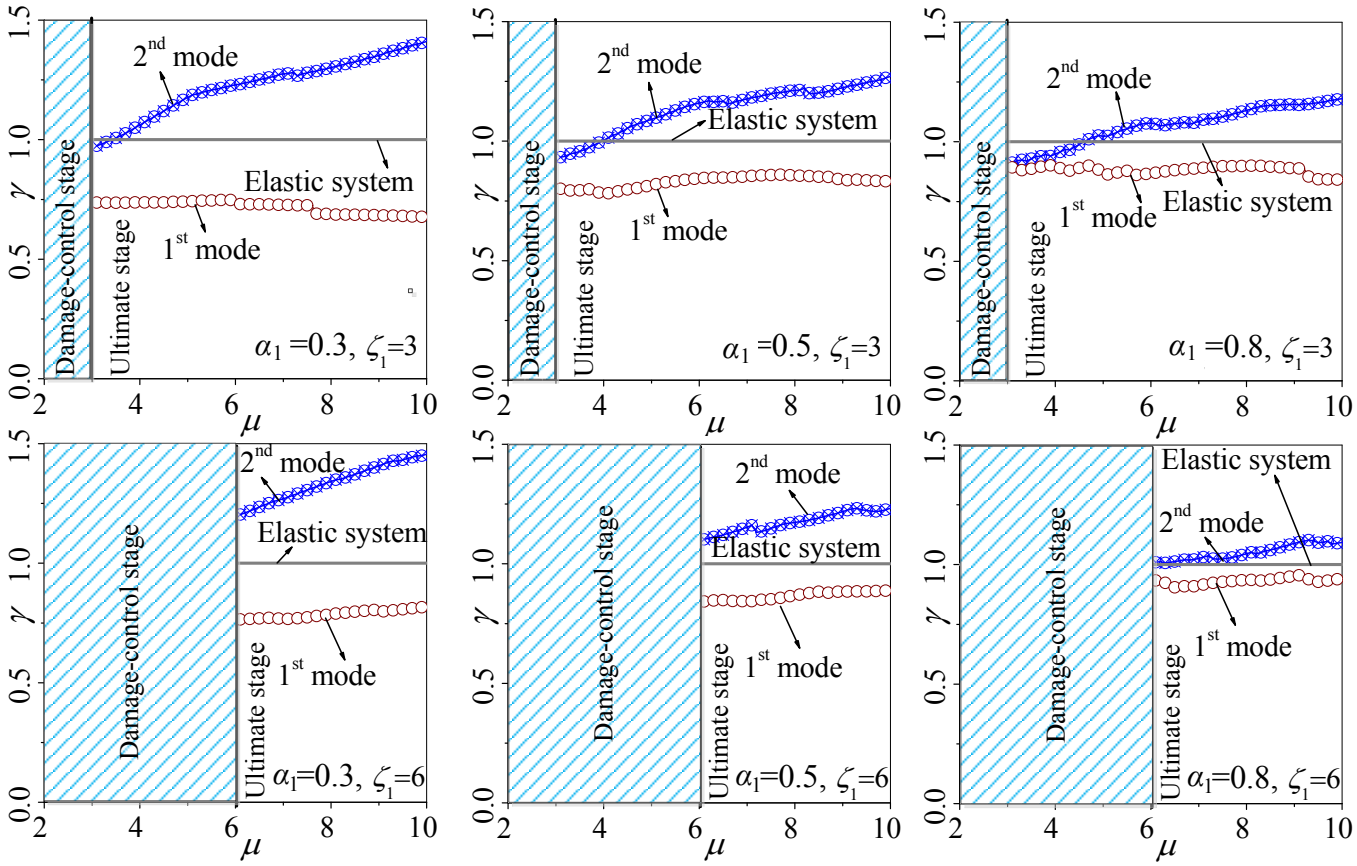

(a)

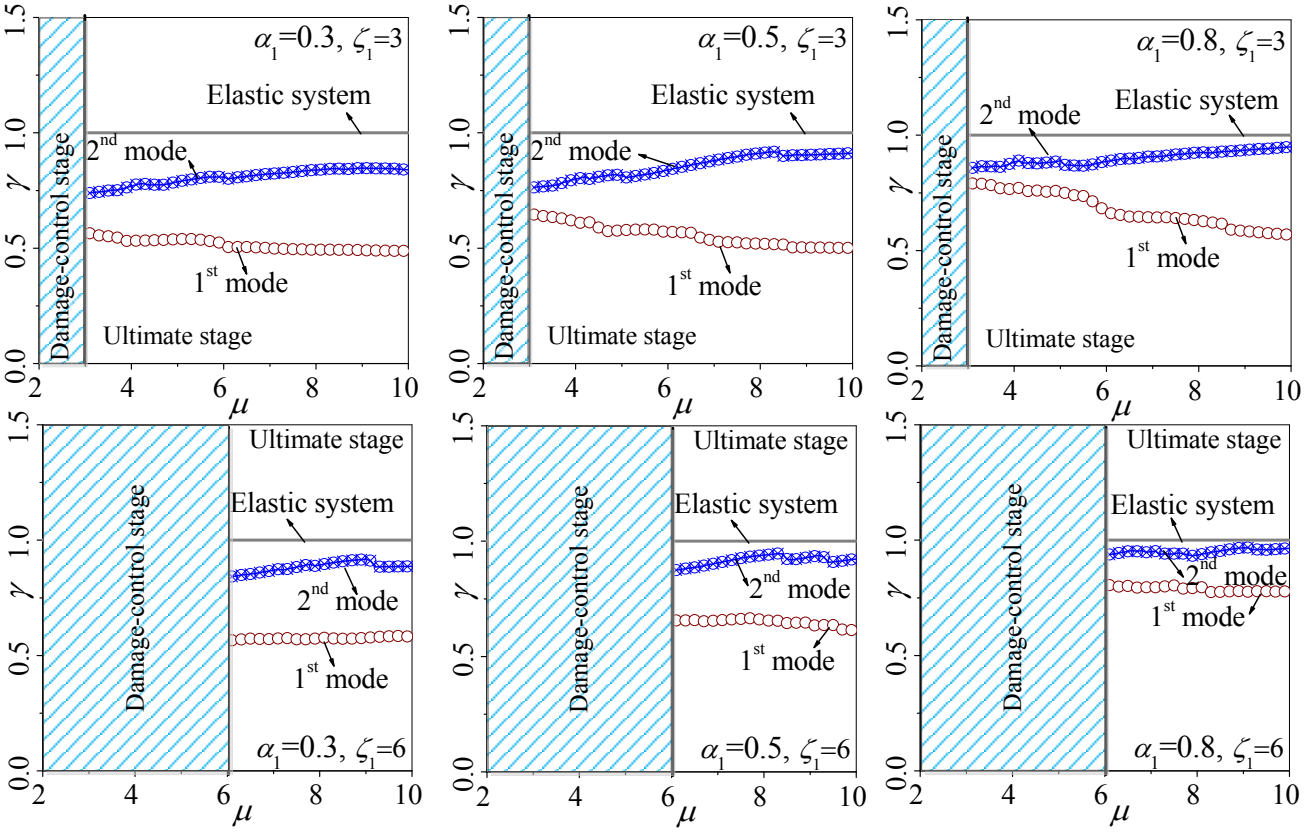

(b)

Fig. 15 Energy factors of oscillators with identical periods of prototype structures and varied hysteretic parameters of the damage-control core: (a) 5-storey structure and (b) 10-storey structure.

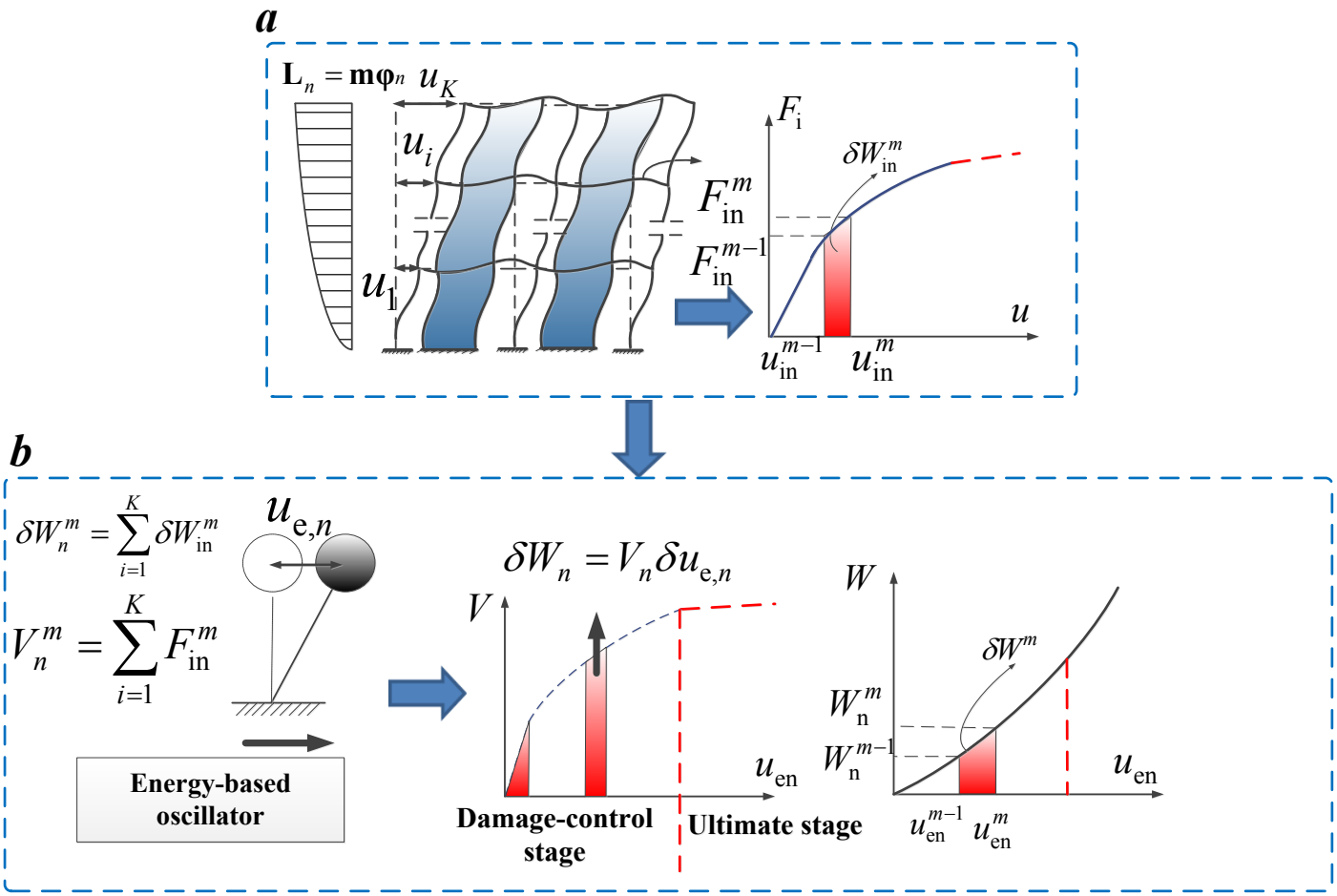

Fig. A1 Procedure of developing capacity curve for an energy-based modal oscillator [38, 40].

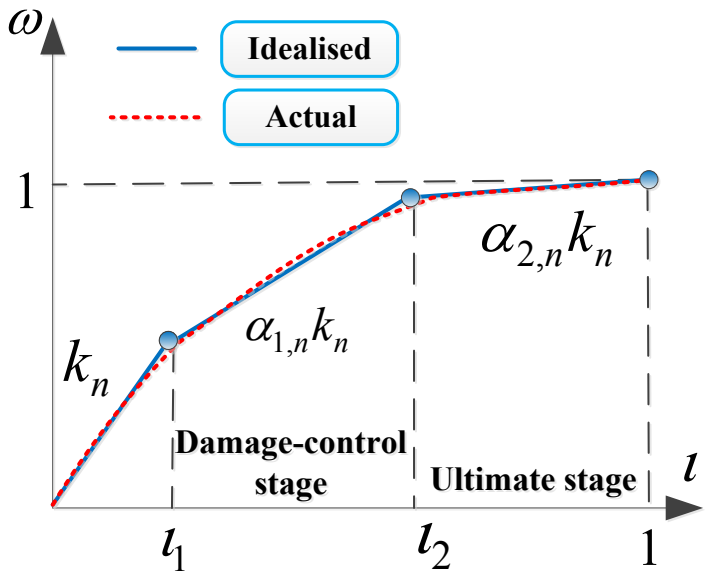

Fig. A2 Trilinear idealisation [3].

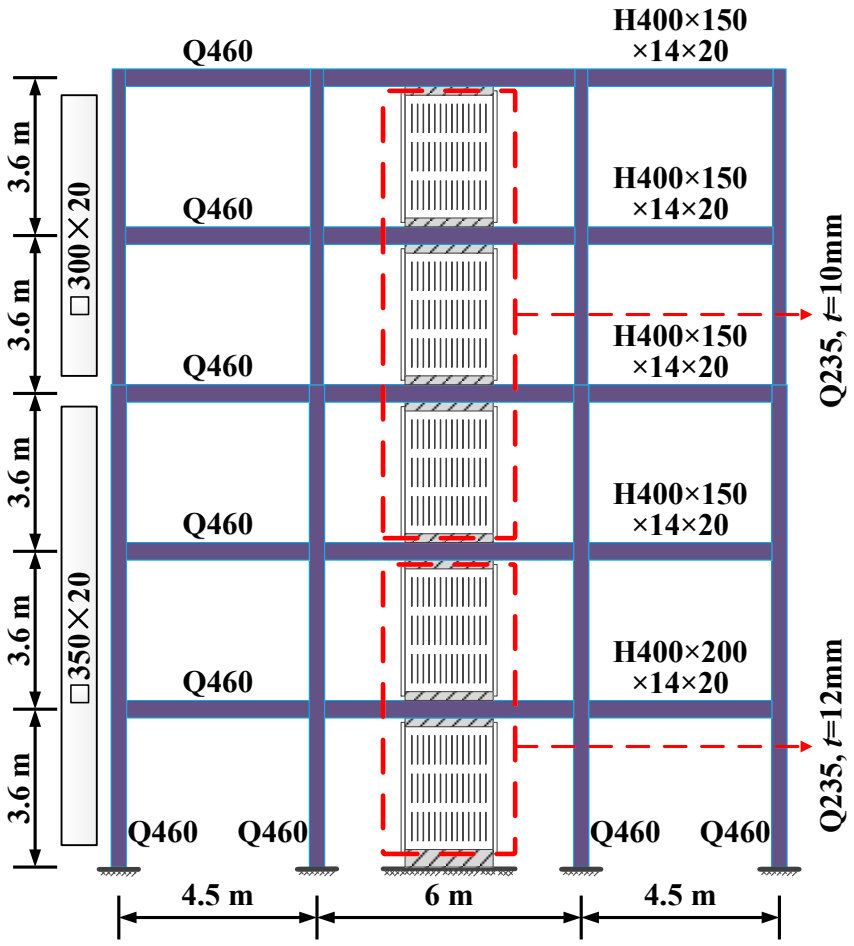
H400×150
×14×20
Q460
H400×150
×14×20
Q460
H400×150
×14×20
Q460
H400×150
×14×20
Q460
H400×200
×14×20
Q460
Q460
Q460
Q460
Q460
3.6 m
3.6 m
3.6 m
3.6 m
3.6 m
□300×20
□350×20
Q235, t=10mm
Q235, t=12mm
4.5 m
6 m
4.5 m

(a)

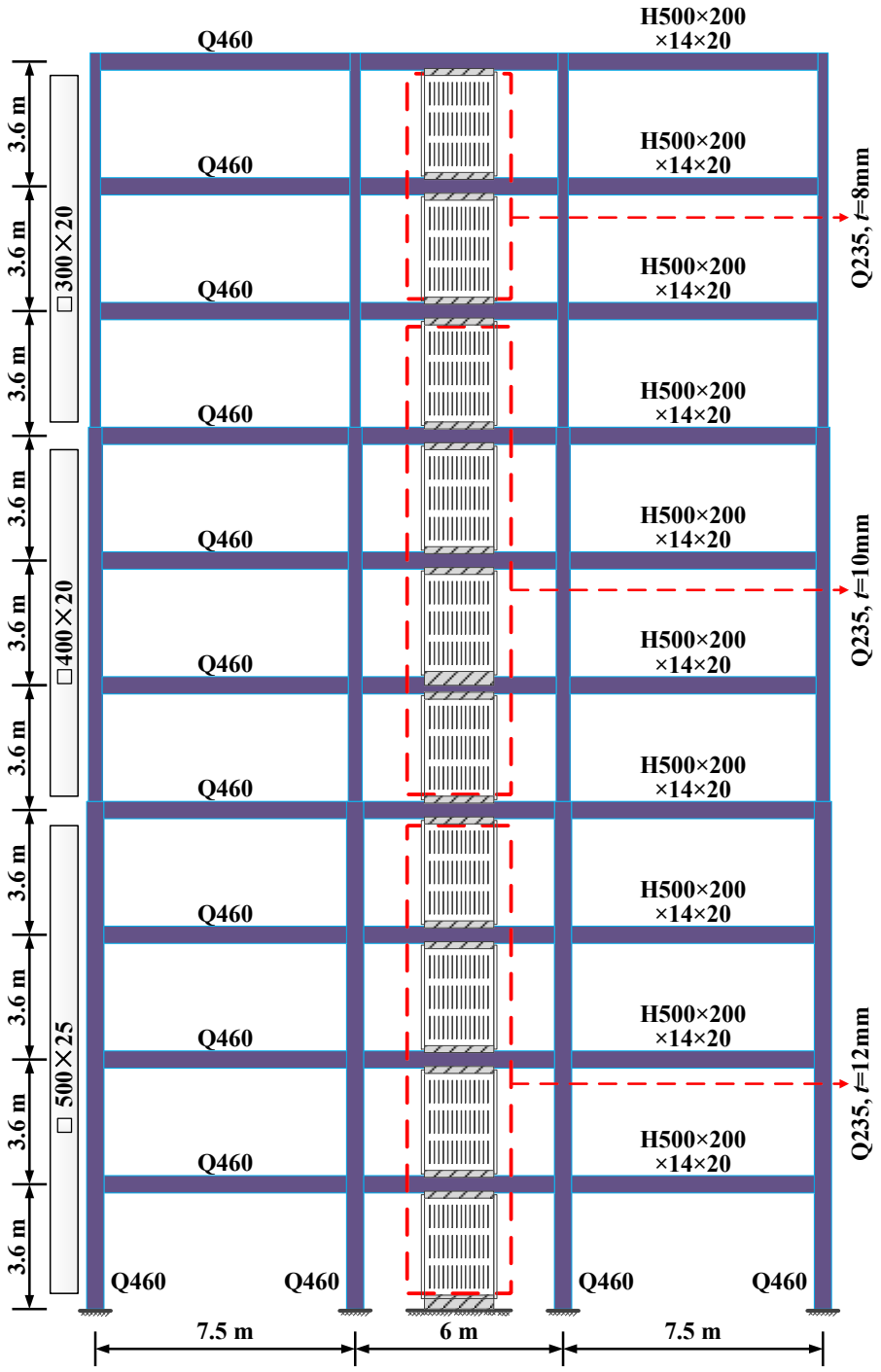

(b)

Fig. B1 Structural arrangement of the prototype structures: (a) 5-storey structure and (b) 10-storey structure.

Table 1 Section information of prototype structures

Floor	*Interior beam*	*Exterior beam*	*Column*	*SSW*				
				b	*h*	*m*	*n*	*t*
5-storey system								
1	I 400×200×14×20	I 400×200×14×20	□350×20	130	650	3	15	12
2	I 400×150×14×20	I 400×150×14×20	□350×20	130	650	3	15	12
3	I 400×150×14×20	I 400×150×14×20	□350×20	130	650	3	15	10
4	I 400×150×14×20	I 400×150×14×20	□300×20	130	650	3	15	10
5	I 400×150×14×20	I 400×150×14×20	□300×20	130	650	3	15	10
10-storey system								
1	I 500×200×14×20	I 500×200×14×20	□500×25	130	650	3	15	12
2	I 500×200×14×20	I 500×200×14×20	□500×25	130	650	3	15	12
3	I 500×200×14×20	I 500×200×14×20	□500×25	130	650	3	15	12
4	I 500×200×14×20	I 500×200×14×20	□500×25	130	650	3	15	12
5	I 500×200×14×20	I 500×200×14×20	□400×20	130	650	3	15	10
6	I 500×200×14×20	I 500×200×14×20	□400×20	130	650	3	15	10
7	I 500×200×14×20	I 500×200×14×20	□400×20	130	650	3	15	10
8	I 500×200×14×20	I 500×200×14×20	□300×20	130	650	3	15	10
9	I 500×200×14×20	I 500×200×14×20	□300×20	130	650	3	15	8
10	I 500×200×14×20	I 500×200×14×20	□300×20	130	650	3	15	8

Table 2 Frequency analysis results of the prototype structures

Structure	*Property* (unit)	*1st Mode*	*2nd. Mode*	*3rd mode*
5-storey structure	Period (s)	0.66	0.22	0.12
	Modal effective mass (t)	236.53	36.66	12.20
	Modal participation factor	1.31	0.47	0.26
10-storey structure	Period (s)	1.36	0.47	0.27
	Modal effective mass (t)	626.41	103.05	36.25
	Modal participation factor	1.36	0.54	0.30